Hybrid cobalt ferrite/carbon catalysts: synthesis, characterization and applications in water treatment

Nathália Maria Costa Guari

Thesis report submitted to

Escola Superior de Tecnologia e Gestão

Instituto Politécnico de Bragança

Master Degree in

Chemical Engineering

Supervisors:

Prof. Helder Teixeira Gomes

Prof. Patricia Hissae Yassue Cordeiro

Dr. Jose Luis Díaz de Tuesta Triviño

Bragança

December, 2020

Hybrid cobalt ferrite/carbon catalysts: synthesis, characterization and applications in water treatment

Nathália Maria Costa Guari

Thesis report submitted to **Escola Superior de Tecnologia e Gestão** of **Instituto Politécnico de Bragança** to obtain a Master Degree in **Chemical Engineering** in the ambit of the double diploma with the **Universidade Tecnológica Federal do Paraná - Câmpus Londrina**

Supervisors:

Prof. Helder Teixeira Gomes

Prof. Patricia Hissae Yassue Cordeiro

Dr. Jose Luis Díaz de Tuesta Triviño

Bragança

December, 2020

In memory of da Costa, O. V.

Acknowledgments

This work developed around one year, not only emphasizes the master's program but it also represents the epiphany of my academic trajectory until this point. In this process, I have many people to whom I'm grateful, too many to name all. My parents Lucrécia and Milton Guari for having provided all the love and necessary support during these years. My fiance Hebert Labbate for being loving, patient, and emotionally supportive. To my friends for encouraging and believing in me.

Thanks to my supervisors, professor Dr. Helder Teixeira Gomes and Dr. Jose Luis Diaz de Tuesta Triviño of Instituto Politécnico de Bragança (IPB) and professor Dr. Patricia Hissae Yassue Cordeiro of Universidade Tecnológica Federal do Paraná (UTFPR) for helping me so much. I appreciate the knowledge given to me. I would also like to thank M.Sc. Adriano Silva, who has helped me during this thesis.

I'm very grateful to all the professors at UTFPR-Londrina, especially professor Dr. Walmir Eno Pottker for being my first mentor and introducing me to scientific research.

This work is a result of Project "RTChip4Theranostics – Real-time Liver-on-a-chip platform with integrated micro(bio)sensors for preclinical validation of graphene-based magnetic nanocarriers towards cancer theranostics", with the reference NORTE-01-0145-FEDER-029394, supported by Norte Portugal Regional Operational Programme (NORTE 2020), under the Portugal 2020 Partnership Agreement, through the European Regional Development Fund (ERDF); and CIMO (UIDB/00690/2020) through FEDER under Program PT2020.

Abstract

This work deals with the development of carbon-coated magnetic cobalt ferrite nanoparticles as catalysts for the treatment of water containing Contaminants of Emerging Concern (CEC) by Catalytic Wet Peroxide Oxidation (CWPO), using paracetamol (PCM) as model pollutant. For this purpose, a magnetic core ($CoFe_2O_4$) is developed by the sol-gel method, the core is subsequently coated with a resin prepared from formaldehyde, resorcinol and tetraethyl orthosilicate (TEOS), and later carbonized by pyrolysis at 600 °C under a N_2 atmosphere. Afterwards, the silica generated from TEOS is removed by etching with NaOH to create a void inside the particle, creating a yolk-shell shape denoted as $CoFe_2O_4$@void@C. XRD, TEM and FTIR analysis revealed that the uncoated core is composed by a $CoFe_2O_4$ cubic spinel structure with space group Fd-3m and a crystallite size of 53 nm, calculated using the W-H method, that matches very well with the average size observed by TEM equals to 53.51 ± 4.2 nm. The average size of the nanoparticles for the hybrid coated ferrite increases to 58.7 ± 8.1 nm. After the preparation of the catalysts, reaction runs were performed to assess its suitability for the degradation of PCM by CWPO. The concentration of paracetamol, hydrogen peroxide and Total Organic Carbon (TOC) were recorded against the reaction time. The performance of the $CoFe_2O_4$@void@C catalyst was compared to that of the uncoated ferrite, the $CoFe_2O_4$ and $CoFe_2O_4$@void@C materials allowing TOC values of 46 and 58% respectively at 24h. The hybrid coated ferrite succeeds in avoid iron leaching and to be a stable catalyst. The amount of leached iron at the end of the treatment was equal to 1.59 $mg \cdot L^{-1}$, which is within the limit concentration of 2 $mg \cdot L^{-1}$ of iron allowed in waters, as established EU regulations. A kinetic model was proposed describing the decomposition of hydrogen peroxide and the removals of the pollutant PCM and TOC with the $CoFe_2O_4$@void@C as catalyst, applying an empirical kinetic model composed of a second-order and an autocatalytic expression to describe the decomposition of H_2O_2 and PCM, respectively. The kinetic model for TOC can be well-described as a sum of the initial pollutant plus the oxidation intermediates from the PCM and the organic components that are refractory to the process.

Keywords: Magnetic nanoparticles; CWPO; Paracetamol; Yolk-shell.

Resumo

Este trabalho trata do desenvolvimento de nanopartículas magnéticas de ferrita de cobalto revestidas com carbono como catalisadores para o tratamento de água contendo contaminantes de preocupação emergente por oxidação catalítica por peróxido úmido (CWPO), usando paracetamol (PCM) como poluente modelo. Para o efeito foi inicialmente sintetizado um núcleo magnético pelo método sol-gel, revestido de seguida com uma resina preparada a partir de formaldeído, resorcinol e tetraethyl orthosilicate (TEOS), posteriormente carbonizada por pirólise a 600 °C sob atmosfera de N_2. Subsequentemente, a sílica gerada a partir de TEOS é removida com NaOH para criar um vazio entre o núcleo e o revestimento, criando uma estrutura de nanopartícula denominada de casca de gema, denotada como $CoFe_2O_4$@void@C. As análises de XRD, TEM e FTIR revelaram que o núcleo é composto por uma estrutura espinélica cúbica de $CoFe_2O_4$ com grupo espacial Fd-3m e tamanho de cristalito de 53 nm, calculado usando o método W-H que corrobora com o tamanho médio observado por TEM igual a 53.51 ± 4.2 nm. O tamanho médio das nanopartículas de ferrite recoberta aumentam para 58.7 ± 8.1 nm. Os catalisadores preparados foram testados na degradação de PCM por CWPO. As concentrações de paracetamol, peróxido de hidrogénio e Carbono Orgânico Total (TOC) foram registradas em função do tempo de reação, sendo o desempenho do catalisador $CoFe_2O_4$@void@C comparado com o da ferrite não revestida. Os catalisadores $CoFe_2O_4$ e $CoFe_2O_4$@void@C alcançaram valores de TOC de 46 e 58% respectivamente, após 24h de reação. No ensaio realizado com a ferrite revestida observou-se uma lixiviação de ferro 1.59 $mg \cdot L^{-1}$, provando ser um catalisador estável, estando a quantidade de ferro no final do ensaio dentro da concentração limite de 2 $mg \cdot L^{-1}$ de ferro permitido em águas, como estabelecido pela legislação da União Europeia. Foi definido um modelo cinético que descreve a decomposição de peróxido de hidrogénio e as remoções do poluente PCM e de TOC, considerando o $CoFe_2O_4$@void@C como catalisador. Foi aplicado um modelo cinético empírico composto por uma expressão de segunda ordem e uma expressão autocatalítica para descrever a decomposição de H_2O_2 e PCM, respectivamente. O modelo cinético para a evolução de TOC pode ser bem descrito como a soma do poluente inicial mais os intermediários de oxidação do PCM e os componentes orgânicos refratários ao processo.

Palavras-chave: Nanopartículas magnéticas; CWPO; Paracetamol;Casca de gema.

LIST OF FIGURES

LIST OF TABLES

LIST OF ACRONYMS

AOP	Advanced oxidation processes
CBZ	Carbamazepine
CS	Core-shell
CWPO	Catalytic wet peroxide oxidation
ECWAO	Electro-assisted catalytic wet air oxidation
FTIR	Fourier transform infra-red spectroscopy
GAC	Granular activated carbon
GbMNPs	Graphene-based magnetic nanoparticles
Hc	High coercivity
HPLC	High performance liquid chromatography
IBP	Ibuprofen
LC	Liquid Chromatography-UV
MB	Methylene blue
MBT	Multi-barrier treatment
MF	Micro-filtration membrane
MNPs	Magnetic nanoparticles
Ms	Saturation magnetization
MS	Mass spectrometry
MWCNT	Multi-walled Carbon Nanotubes
NPs	Nanoparticles
Oe	Oersted
PCM	Paracetamol
RF	Resorcinol-formaldehyde
SCS	Solution Combustion Synthesis
TCS	Triclosan

TEM	Transmission electron microscopy
TEOS	Tetraethyl orthosilicate
TOC	Total organic carbon
WWTP	Wastewater treatment plant
XRD	X-ray Diffraction
YS	Yolk-shell

TABLE OF CONTENTS

Chapter 1: Introduction

1 INTRODUCTION

Due to their importance in catalysis, previous studies on ferrite nanoparticles, MFe_2O_4 (M= Ni^{2+}, Fe^{2+}, Co^{2+}), have intensively investigated its structural and morphological properties, as well as the synthesis procedures. For example, $CoFe_2O_4$, when used as a water treatment catalyst [1,2], has shown remarkable chemical stability, large magnetic anisotropy, moderate saturation magnetization and predominantly ferromagnetic behavior [1–4]. These characteristics contribute to easy separation of the catalyst from the water matrices at the end of treatment, upon application of a magnetic field through the system [5–7]. In general, ferrites act not only in water catalytic treatment processes, but also in the controlled release of drugs [8,9] and, due to its ferromagnetic characteristics, in nuclear magnetic resonance as a contrast agent [10].

There are several methods to produce ferrites, such as co-precipitation [11], hydrothermal synthesis [12], combustion [13], solution combustion synthesis [14] and sol-gel [3], among others. In this work, the sol-gel method was chosen due to the high reproducibility of the technique, the control of the structural and morphological properties, as well as the certainty of obtaining a magnetic nanomaterial with high crystallinity [15,16,3]. After the sol-gel synthesis, heat treatment is necessary to ensure that there are no impurities or organic compounds left in the final material, as well as thermo-stability.

The scientific community has been investigating the effects of using carbon to coat the catalysts used in industrial water treatment. This interest is due to the specific properties of carbon as stable agent in basic and acidic media, its high surface area, that allows high dispersion and stability for supported metals, as well as the possibility to control the morphological properties of the final composite [9,17,18]. However, the most important properties are the increase of the catalyst recovery rate and the elimination/reduction of metal leaching from the catalyst to the treated waters.

Currently, natural water matrices have been compromised by wastewater generated at industrial plants, due to the presence of toxic pollutants that cannot be removed by conventional biological processes. Within this context, Advanced Oxidation Processes (AOPs) have emerged as technologies able to oxidize a wide range of organic pollutants contained in wastewater that are refractory to be handled by biological processes. AOPs are defined as treatment solutions relying on the use of hydroxyl radicals ($HO^{\bullet}$) produced from different chemical agents, such as H_2O_2, ozone, metal oxides and

auxiliary energy sources like ultraviolet-visible light. Due to the high oxidizing power of hydroxyl radicals ($HO^{\bullet}$), AOPs may lead to the decomposition of organic compounds into minerals such as H_2O and CO_2. Hence, the main advantage of these processes is to convert toxic organic streams into more biodegradable forms as achieved in this work [1,2,17].

Different types of AOPs have been developed over the years, such as photocatalysis, ozonation, cavitation, Fenton-like process, electrochemical oxidation and intensification by the combination of these processes (*e.g.* photo-Fenton)[19,20]. The Fenton process deals with the use of H_2O_2, which is decomposed into $HO^{\bullet}$ in the presence of Fe^{2+}, acting as a homogenous catalyst. The main drawbacks of this process are the continuous feeding of the iron catalyst and the generated sludge containing iron, leading the research community to develop heterogeneous catalysts for a process known as heterogeneous Fenton, Fenton-like or Catalytic Wet Peroxide Oxidation [17,21]. Under this context, the present work is aimed to develop catalyst composites composed of cobalt ferrite nanoparticles coated with carbon for application in the CWPO of water streams containing pharmaceutical compounds.

1.1 Objectives

The main objectives of this study are the synthesis and assessment of carbon-coated magnetic cobalt ferrite nanoparticles as potential catalysts for the CWPO of Contaminants of Emerging Concern (CEC), considering paracetamol as model pollutant.

Initial tests for structural, stability and morphological analysis were carried out by X-ray Diffraction (XRD), Transmission Electron Microscopy (TEM) and Fourier Transform Infrared Spectroscopy (FTIR). The catalytic activity of the materials were assessed in the CWPO of paracetamol at mild conditions. A non-catalytic run (wet peroxide oxidation of paracetamol in the absence of catalyst) and pure adsorption tests of paracetamol on the synthesized materials (in the absence of H_2O_2) were conducted in order to compare their contributions and guarantee the catalytic activity of the materials in CWPO. Finally, this study attempts to define a kinetic model that describes the decomposition of hydrogen peroxide and the removal of the pollutant paracetamol and Total Organic Carbon (TOC).

Chapter 2: State of the Art

2 STATE OF THE ART

2.1 Nanoparticles

Nanotechnology is a large and diverse area for research due to different types of nanoscaled structured materials, such as polymers, metals, biomaterials and others. The main concern of this area is the controlled synthesis of these nanometric structures, and their subsequent arrangement, to form the nanostructured materials for several possible applications. At nanoscale dimensions, new phenomena appear that is not occurring at the macro-scale, since nanoparticles have different chemical and physical properties than macroscopic ones. The new properties that arise at the nanoscale can be described by two main effects resulting from the formation of nanostructures: size effects and effects induced by the increase in surface area, respectively [22,23, 41, 42].

Size effects are described by quantum effects, where the normal electronic structure is replaced by a series of discrete electronic levels. The increase in the surface area of nanomaterials causes a significant increase in their reactivity, performing an eminent role in chemical processes, especially in heterogeneous catalysis, since is observed an increase of catalytic sites at the catalyst surface [22,23,24].

In most applications, particles perform better when their size is lower than a critical value, which is material dependent, but generally around 10-20 nm [25]. Each nanoparticle has a large constant magnetic moment and has a fast response to an applied magnetic field with residual magnetism and Coercivity (Hc) [26]. Coercivity is the minimum value of magnetizing intensity that is required to bring the material to its original state. In the case of a ferromagnetic substance, such as cobalt ferrite, if the applied magnetic field is increased in the reverse direction, the substance completely loses its magnetization at some point Hc. This point is known as coercivity [15, 22].

The magnetic nanomaterial selected in this work is cobalt ferrite $CoFe_2O_4$, which has different properties from those in other ferrites, such as nickel ferrite ($NiFe_2O_4$), or in iron oxides, magnetite (Fe_3O_4) and maghemite (Fe_2O_3). Among those properties, $CoFe_2O_4$ has high coercivity (about several hundred Oe [27, 28]), good chemical stability and high mechanical hardness [29]. However, the structural, chemical and morphological characteristics are dependent on the experimental conditions and the methodology employed in the synthesis.

2.1.1 Crystal structure of ferrites

Ferrites are a class of varied iron oxides present in their crystalline structure together with Fe^{3+} ions. The scientific community has been studying a diversity of divalent cations, such as Fe^{2+} (Fe_3O_4), Ni^{2+} ($NiFe_2O_4$), Cd^{2+} ($CdFe_2O_4$ - cadmium ferrite), Mg^{2+} ($MgFe_2O_4$ - magnesium ferrite), Co^{2+} ($CoFe_2O_4$), Cu^{2+} ($CuFe_2O_4$ - copper ferrite) and Zn^{2+} ($ZnFe_2O_4$ - zinc ferrite) [30]. Ferrites can present different types of crystalline order, such as cubic, orthorhombic or hexagonal, just to name a few. The orders are according to the position of atoms in the structure [31]. Among the class of cubic ferrites, the ferrites in block d are among the most used in nanotechnology applications, because of their high response a magnetic field and stability. Ferrites in block d have a spinel structure of $CuFe_2O_4$ and $ZnFe_2O_4$, and inverse spinel of Fe_3O_4 and $CoFe_2O_4$ [30].

The crystal structure is a description of the ordered arrangement of atoms in a crystalline material. Ordered structures occur from the intrinsic nature of the constituent particles to form symmetric patterns that repeat along the principal directions of three-dimensional space in matter. The smallest group of particles in the material that constitutes this repeating pattern is the unit cell of the structure. The unit cell completely reflects the symmetry and structure of the entire crystal [32,53]. Figure 1 shows the unit cell of $CoFe_2O_4$.

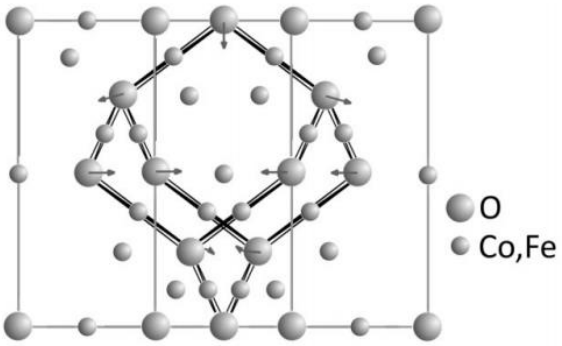

Figure 1. Unit cell of $CoFe_2O_4$ with spinel crystal structure and space group of Fd-3m [32]

Cobalt ferrites possess an inverse spinel structure, where the tetrahedral sites (A-sites) as well as half of the octahedral sites (B-sites), are occupied with Fe^{3+} ions, while Co^{2+} ions are distributed over the octahedral B-sites [33].

2.2 Methods of Synthesis

The research on nanoparticles include the development of magnetic materials with different composition types and phases, including pure metals Fe, Ni, Co, oxides such as Fe_3O_4 and ferrites $CoFe_2O_4$, $NiFe_2O_4$ and $MgFe_2O_4$, among others [24]. In recent years, several publications reported efficient routes for the synthesis of nanomaterials with controlled size, morphology, high stability and homogeneity. Popular methods include hydrothermal synthesis, co-precipitation, solution combustion synthesis and sol-gel[9,13,34,35]. All of these routes can enable high-quality magnetic materials.

2.2.1 Hydrothermal synthesis

Hydrothermal synthesis is performed in aqueous media at high pressure and high temperature, involving the hydrolysis and condensation of a metal salt to produce magnetic nanoparticles [34,36].

Wang et al.[36] prepared hydrophilic monodispersed $CoFe_2O_4$ nanoparticles with a crystalline phase and uniform sizes between 9 and 12 nm by hydrothermal reduction. Their system is a generalized hydrothermal method to synthesize a variety of different nanocrystals by a liquid-solid-solution reaction, as illustrated in Figure 2.

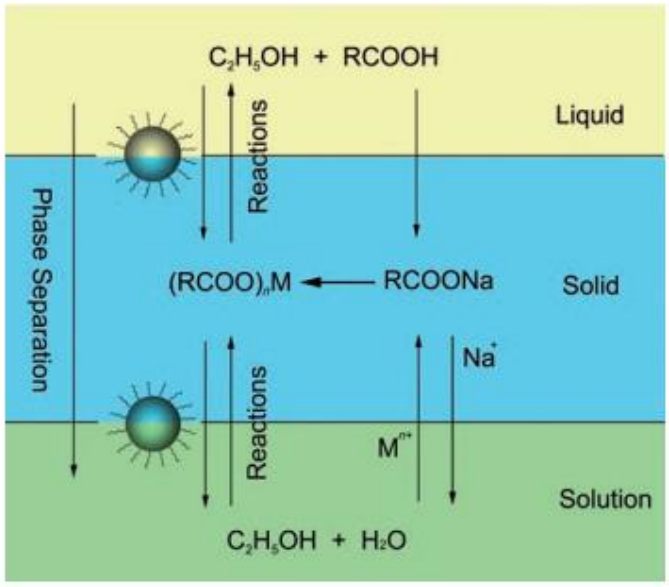

Figure 2. Scheme of a liquid–solid–solution reaction [36]

Figure 2 shows the method considering the use of a metal linoleate, an ethanol-linoleic acid liquid phase and a water-ethanol solution at different reaction temperatures

under high-pressure conditions. The solvents used were ethylene glycol, sodium acetate and polyethylene glycol. Ethylene glycol served as a high boiling reducing agent known as the polyol process to produce monodispersed metal nanoparticles or metal oxides. Wang et al. did another important test. They reported how cobalt ferrite can be recovered at the end of the process using magnetic separation, as shown in Figure 3.

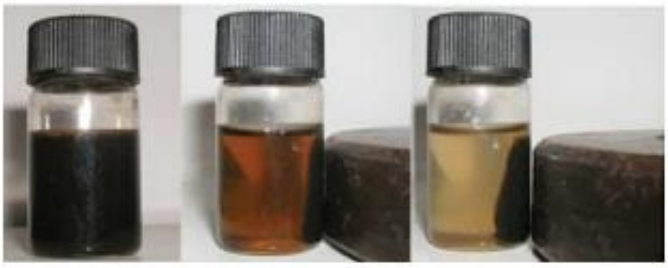

Figure 3. The separation of $CoFe_2O_4$ nanocrystals from the solution by the action of a magnetic force [36]

2.2.2 Co-precipitation

Co-precipitation is a convenient and easy route to synthesize iron oxides and ferrites. The precursors are generally Fe^{2+} and Fe^{3+} salts dissolved in aqueous solutions by the addition of a base under an inert atmosphere. The synthesis can be carried out either at room temperature or at high temperature. The material morphology, composition and crystallinity depend on the anion (sulfates, nitrates or chlorides), reaction temperature, Fe^{2+}/Fe^{3+} ratio, pH value and average ionic strength. The saturation magnetization values are generally less than 30 to 50 emu·g^{-1} when it is compared to bulk material (90 emu·g^{-1}) [11,37,38].

2.2.3 Solution Combustion Synthesis

Solution Combustion Synthesis (SCS) is seen as a chemical-soft and economically favorable route in the production of fine powder nanoparticles. This method involves a redox reaction of an oxidant with a fuel in the presence of metal cations. Oxidants are usually precursors of metals such as nitrates and chlorides. The fuel is any organic compound, such as urea, glycine and citrus, capable to form complexes with metal ions. Generally, SCS consists in three steps, the formation of the combustion mixture, then the formation of the gel and finally the combustion of the gel [13,14].

One of the options for SCS is to consider plant extracts, to be used as fuel in the chemical reactions of solutions containing Fe^{2+} and Fe^{3+}. However, the control over material phases, stoichiometry and morphology can be difficult since the precursors are not pure [39].

2.2.4 Sol-gel

The sol-gel method provides a route for the synthesis of nanomaterials with high-temperature resistance, ferromagnetic behavior, homogeneity and control in the nano scale. The sol-gel synthesis is a multistep process which involves the conversion of a precursor solution into a sol or a gel, then subsequently transitioning the gel to an oxide compound. The homogeneity of the final product is determined by the distribution of cations in the gel. Therefore, it is extremely important that the reaction precursors are capable to form a homogeneous multicomponent gel without any phase segregation during the sol-gel transition [3,16,35,40].

Cobalt ferrite synthesis by sol-gel is usually performed with the following steps: mixing, gelation, drying and heat treatment [3,16,35,40], as detailed in the following:

1. Mixing: the process begins by mixing an alcohol solution and a metal alkoxide catalyst (M), such as nitrates or chlorides in an aqueous network. Generally, in this part, a hydrolysis reaction occurs followed by poly condensation, as shown in reactions (1), (2) and (3) [3,16,35,40].

   Hydrolysis reaction

   $$M(OR)_n + nH_2O \rightarrow M(OH)_n + nROH \quad (1)$$

   Poly condensation reaction

   $$M(OH)_n \rightarrow MO_{\frac{n}{2}} + \left(\frac{n}{2}\right) H_2O \quad (2)$$

   Poly condensation reaction for the formation of $CoFe_2O_4$

   $$2Fe(OH)_3 + Co(OH)_2 \rightarrow CoFe_2O_4 + 4H_2O \quad (3)$$

2. Gelation: the growth from the grouping of the polymeric units to form a continuous three-dimensional network of particles. From this point on the transition from the sol to the gel phase takes place [3,16,35,40].

3. Drying: during drying occurs the removal of liquid in the pores of the gel. The process consists on a slow evaporation of the solvent, producing the so-called xerogels, that are higher in density than gels [3,16,35,40].
4. Heat treatment: this is the transformation of the gels into denser materials. The treatment helps in the elimination of unwanted radicals and pores which ensures the use of the material at high temperatures without changes in structure [3,16,35,40].

Giannakopoulou et al.[3] prepared Ni-ferrite at different temperatures by the sol-gel method, using nitrates, ethanol and ethylene glycol as precursor. Table 1 and Figure 4 show the results of the density and of the particle size determined by XRD. It can be observed that the particle size increases with the rise of the annealing temperature. The intensification of the annealing temperature is the heat treatment that is cited above, which leads the ferrites to higher surface area and stability against futures fractures.

Table 1. Samples of $NiFe_2O_4$ annealed at different temperatures [3].

No.	Annealing temperature (°C)	Density ($g.cm^{-3}$)	Crystal size estimate (nm)
N3	300	5.37	15
N6	600	-	20
N9	900	5.36	50
N11	1100	5.37	(>>)
N16	1600	5.37	(>>)

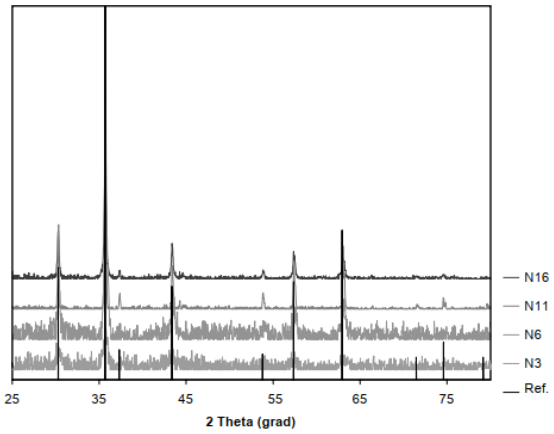

Figure 4. XRD spectra of samples N3, N6, N11 and N16 shown in Table 1, corresponding to $NiFe_2O_4$ nickel iron (III) oxide, Y-axis is arbitrary units [3]

Hashemi et al. [33] prepared $CoFe_2O_4$ nanoparticles by a sol-gel auto-combustion method in the simultaneous presence of ethylene glycol and agarose as complexing agents and nitrates as precursors to analyze their effects on the structure, morphology and magnetic properties of the developed nanoparticles. The samples with the equivalence ratio Chemical reagents/Nitrates of 1 and 2 obtained a crystallite size of 28 ± 3 and 24 ± 0.5 nm respectively. The authors revealed that the saturation magnetization and coercivity could simultaneously be increased by the proper addition of ethylene glycol and agarose so that these magnetic properties could be used for many applications as sensing devices, drug delivery or recovery of catalyst in heterogeneous catalysis.

Sinkó and Mezei [41] performed tests with different precursors for the synthesis of aluminosilicate gels. The salts tested were aluminum nitrate and aluminum chloride, while the solvents tested were ethylene glycol, methanol, ethanol, 1-propanol and 2-propanol. In their paper, the collaborators concluded that aluminum nitrate was the best precursor. Among the reasons why, it was given that the extent of Al incorporation into the gel network was much lower in chloride containing gels than in nitrate containing gels. The gel structure obtained with Al chloride was not homogeneous. It was dominated by a silica network with fractal-like structures strongly deformed by unbounded Al content. Unbounded Al content is associated with hydrated Al (III) ions connected by weak hydrogen bonds that can result in phase separation. Regarding the solvent, the best results vary according to the desired molar ratio for the aluminosilicate gel.

2.3 Protection and stabilization of magnetic nanoparticles

Stability is a critical requirement for any application of magnetic nanoparticles, including their application as catalysts. Therefore, strategies should be developed to create resistance on these nanomaterials related to agglomeration, precipitation and leaching. Usually, the protection used is a core-shell (CS) structure to isolate the nanomaterial from the environment. The applications of these techniques are divided into two mains groups: the coating with organic materials and the coating with inorganic materials. Polymers are among the most extensively used organic materials. For inorganic materials, silica, carbon or precious materials, such as Ag and Au, are used [37,38,42].

Yolk-shell (YS) appeared as a core-shell development. YS is a hybrid structure consisting of a movable core inside a hollow shell of the same or different materials. The

principal difference between the core-shell and the yolk-shell structure is the presence of a void space created from a sacrificial layer, giving rise to multifunctional properties [8,43]. Among the characteristics that make YS nanoparticles unique are:

- YS nanoparticles can be synthesized even from a single material to enhance the specific surface area [1,9,43–45];
- The core surface is unblocked compared to nanoparticles synthesized by CS, so the YS NPs provide more active sites and higher surface area [1,9,43–45];
- The void space is suitable to accommodate guest molecules [1,9,43–45];
- The shell layer provides more active inner and outer surfaces [1,9,43–45];
- The void space provides space for the expansion of core NPs in many applications, such as biomedical, catalysis, adsorbents, lithium batteries, among others [1, 9, 37, 39–41].

The yolk-shell nanoparticles can be classified as spherical and non-spherical, depending on their morphology. The spherical YS nanoparticles have five classes, as shown in Figure 5: single-core/shell, multi-cores/single shell, single core/multi-shell, multi-cores/shells and multi-shells [43].

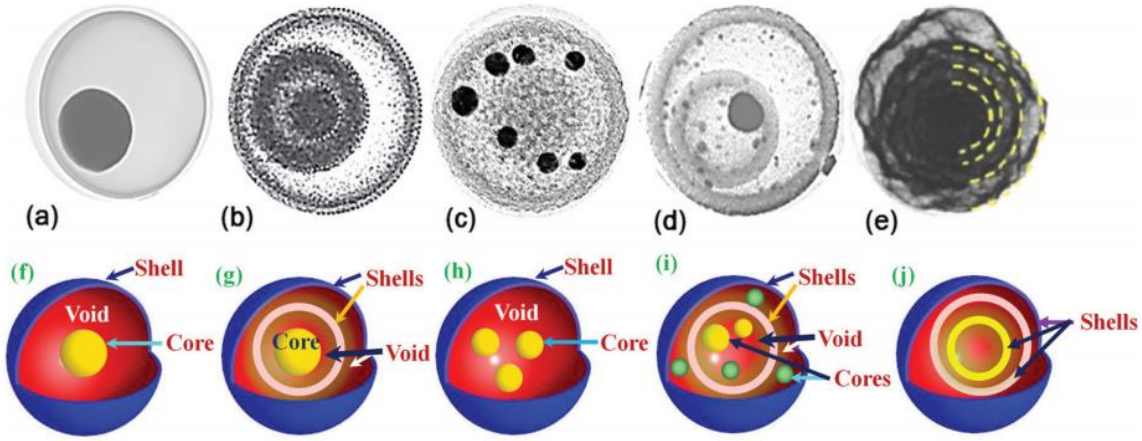

Figure 5. Different classes of spherical yolk-shell NPs (a) single-core/shell, (b) single core/multi-shell, (c) multi-cores/single shell, (d) multi-cores/shells and (e) multi-shells [43]

2.3.1 Carbon shell

Due to the high stability and biocompatibility of carbon, when recovering a magnetic core with a carbon shell it is possible to obtain thermally stable magnetic nanomaterials with high stability against oxidation and acid leaching. In addition, it is possible to tune the hydrophobicity and hydrophilicity nature of the carbon shell to help

in the diffusion of more hydrophobic and hydrophilic molecules into the core region of the catalyst, which increases its activity [1,8,45,46].

In addition to the benefits of the use of carbon in magnetic composites, due to its porosity and high surface area, carbon materials are also used as adsorbents. However, the separation of nanoscale particles from the suspension after the adsorption process restricts its practical use. To solve this problem, the incorporation of the magnetic core inside the hollow carbon shell, allows the magnetic separation of the nanoparticles from the suspension. Oxide metals are among the metal cores that can be used, such as $CoFe_2O_4$, $NiFe_2O_4$, $MgFe_2O_4$ and Fe_3O_4 [1,8,45,46].

The Stöber [47] method to produce silica spheres of uniform size is frequently used to achieve a carbon shell by the hydrolysis and condensation of silicon alkoxides, such as Tetraethyl orthosilicate (TEOS), in a water-ethanol mixture in the presence of ammonia as catalyst. Nowadays this procedure has been extended to the formation of monodispersed polymeric spheres of resorcinol-formaldehyde (RF). Due to the hydrolysis polymerization reaction mechanism, the organic sol-gel of RF resins is analogous to the silicate sol-gel process [8,9].

Rodrigues et. al [8] developed a protocol to synthesize Yolk-Shell graphene-based nanoparticles with a magnetic core (Fe_3O_4, $NiFe_2O_4$ and $CoFe_2O_4$) for drug delivery applications. Figure 6 depicts the synthesis of the nanoparticles, which was divided into two stages. The synthesis of the magnetic core and then the graphene-based shell. Following a co-precipitation method, the iron oxide core was synthesized. Subsequently, the graphene-based shell was accomplished by hydrolysis and polymerization of the precursors, resorcinol, formaldehyde and TEOS. The authors tested the production of Graphene-based Magnetic Nanoparticles (GbMNPs) with different hollow cavities between the shell and the magnetic core, starting with different concentrations of precursors, as shown in Table 2. The polymerization products, GbMNPs, were washed and annealed under a N_2 flow in a tubular vertical oven at 120 and 400 °C. Then, the silica was removed by etching in a strongly basic NaOH solution resulting in the YS nanostructure. The last step was to achieve hydrophilic GbMNPs to perform drug delivery studies. For that, the graphene-based shells were chemically functionalized by an acid treatment at mild conditions.

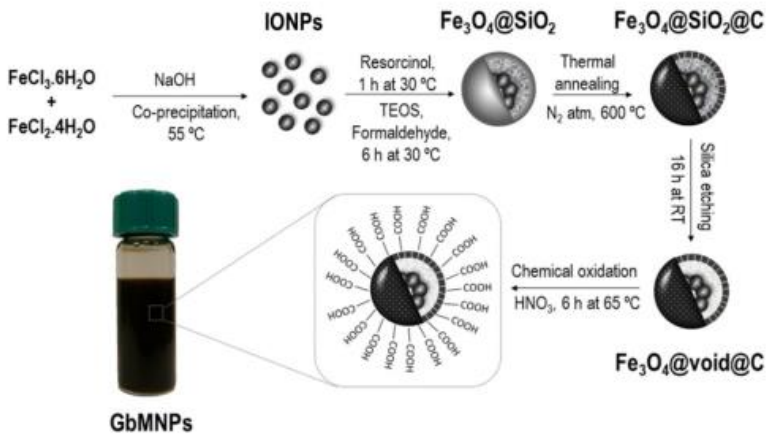

Figure 6. Schematic representation of the steps involved in the development of graphene-based yolk-shell magnetic nanoparticles [8]

Table 2. The effect of the amount of precursors in the synthesis of graphene-based yolk-shell magnetic nanoparticles [8].

Material	Magnetic Core (g)	Resorcinol (g)	Formaldehyde (mL)	TEOS (mL)	Hollow thickness (nm)	Carbon-Shell thickness (nm)
GbMNP-1	0.25	0.05	0.075	0.10	Not detected	1.41 ± 0.44
GbMNP-2	0.25	0.10	0.150	0.21	0.70 ± 0.30	3.55 ± 1.27
GbMNP-3	0.25	0.20	0.300	0.41	2.07 ± 0.92	7.07 ± 1.88

Thus, the results achieved by the authors [8], as seen in Table 2, have shown the capability to synthesize GbMNPs with very distinctive physicochemical and morphological properties just by adjusting the number of carbon precursors. Due to the higher amount used of resorcinol and formaldehyde, a proportionally higher carbon-shell thickness was achieved. There is a desire to attain the highest carbon-shell thickness possible to avoid iron leaching and increases the surface of the materials.

2.4 Advanced Oxidation Processes

The development of new efficient and economically viable technologies for water treatment has been widely investigated. For the treatment of toxic effluents such as antibiotics, personal care products, metabolites, pesticides and effluents from textile industries, Advanced Oxidation Processes (AOPs) appear as an answer with low cost and relative ease of reproduction [20,48–51].

Among the advantages most associated with AOPs are:

- AOPs are not specific techniques, therefore they can be used for the degradation of substrates of any chemical nature, particularly for the degradation of refractory contaminants whose biological treatment can be made possible by partial advanced oxidation [20,49,51,52];
- AOPs can be applied to reduce the concentration of compounds formed in pre-treatment steps such as halogenated aromatics formed during conventional disinfection [53];
- AOPs can be applied in the treatment of contaminants whose concentrations are at low ppb [54];
- In most cases, AOPs do not generate waste, except for some processes that may involve precipitation [20].

Among AOPs, Catalytic Wet Peroxide Oxidation (CWPO) is a technique that can be characterized by the employment of hydrogen peroxide (H_2O_2) as an oxidation source, with a suitable catalyst to promote its partial decomposition into hydroxyl radicals ($HO^{\bullet}$). Magnetic materials can be applied directly as catalysts or included in different support/hybrid materials in CWPO [20,49,51,52].

2.4.1 The Fenton Processes

Fenton in the 19th century demonstrated the oxidation of tartaric acid by the interaction of small amounts of Fe^{2+} with oxidizing agents, including H_2O_2 as the better agent [48,55].

After Fenton's advances, Harber and Weiss reported, in the 20th century, how the reactions of H_2O_2 generate the radicals $HO^{\bullet}$ with a radical anion of oxide $O_2^{\bullet-}$. According to the authors, the interactions between H_2O_2 and Fe^{2+} in an acid medium resulted in the decomposition of hydrogen peroxide through the oxidation of Fe^{2+} into Fe^{3+} with the formation of hydroxide ions and hydroxyl radicals [20,53], as given in Eq. (4) and (5).

$$H_2O_2 + O_2\bullet- \leftrightarrow HO\bullet + OH^- + O_2 \quad (4)$$

$$H_2O_2 + Fe^{2+} \leftrightarrow HO\bullet + OH^- + Fe^{3+} \quad (5)$$

In the 1950s, Barb et al. [56] proposed one of the first Fenton mechanism to demonstrate the participation of Fe^{2+} as catalyst in the oxidation process in two steps.

In a first step, H_2O_2 reacts with $HO^{\bullet}$ in solution, resulting in the formation of hydroperoxyl radicals ($HOO^{\bullet}$) and water as shown in Eq. (6).

$$H_2O_2 + HO\bullet \rightarrow HOO\bullet + H_2O \quad (6)$$

Subsequently $HOO^{\bullet}$ reduces Fe^{3+}, regenerating Fe^{2+} and closing the catalytic cycle, a represented in equation (7).

$$Fe^{3+} + HOO\bullet \rightarrow O_2 + H^+ + Fe^{2+} \quad (7)$$

However, the Fenton process possesses some important unfavorable factors:

- Difficult recuperation or elimination of ions Fe^{3+}/ Fe^{2+};
- Meaningful production of sludge in the form of $Fe(OH)_3$ [1,17,26,53,57];
- High cost of the sludge treatment, accounting to up to 50% of the total costs [1,17,26,53,57];
- The final solution has to be neutralized before returning to the environment, since the Fenton process operates in pH acidity between 2.5 – 4 [1,17,26,53,57].

2.4.2 Catalytic Wet Peroxide Oxidation

As an attempt to remediate the drawbacks of the Fenton process, the use of heterogeneous catalysts become an important quest. Catalysts containing iron supported on carbon materials have been used extensively in CWPO. Equations 8 and 9 describe the multiple possibilities of the state of oxidation of metals (M) contained in heterogeneous catalysts [1,21,52,58].

$$H_2O_2 + M^{n+} \leftrightarrow HO\bullet + M^{(n+1)+} + HO^- \quad (8)$$

$$M^{(n+1)+} + H_2O_2 \rightarrow M^{n+} + HOO\bullet + H^+ \quad (9)$$

Although the general reactions are described above, the process is much more complex and includes many other reactions. In the last decade, the scientific community has been working to develop techniques to optimize this process.

Figure 7 schematizes the use of heterogeneous catalysts in CWPO. In this example, the hybrid carbon material can promote the decomposition of hydrogen peroxide into hydroxyl radicals, which are responsible for oxidizing the pollutants. In this

case, the catalyst can be recovered at the end with the application of a magnetic field. Also, if the catalyst is stable enough, it can be used again in another CWPO run.

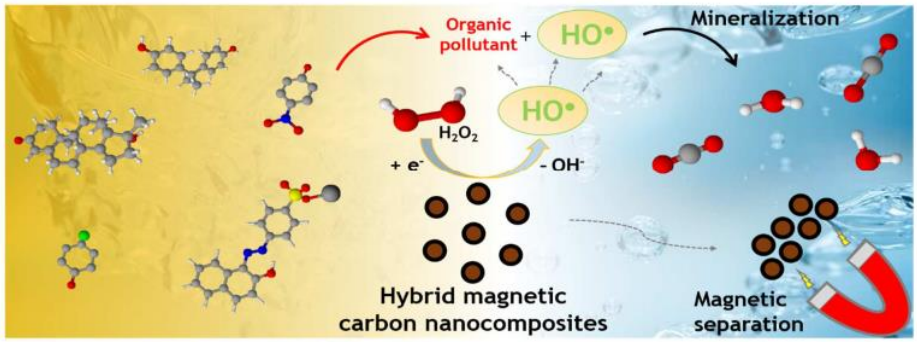

Figure 7. Catalytic wet peroxide oxidation: a route towards the application of hybrid magnetic carbon catalysts [17]

Wang et. al. [57] were researching how powerful the Fenton-based reaction is in breaking down refractory organic pollutants, but found it to be limited to a low pH range. As a proposal, the authors presented Fe_3O_4-Multi-Walled Carbon Nanotubes (MWCNT), because of carbon nanotubes have a remarkable feature of a large specific surface area, hollow and layered structures and the sp^2 hybridized carbon bonds in MWCNTs enables them to be a good electronic transfer support. After obtaining the Fe_3O_4-MWCNT hybrid via *in situ* growth of Fe_3O_4 MNPs on the surface of the MWCNTs, they tested it as catalyst for H_2O_2 reduction. The authors prepared the nanocomposites to remove a typical organic dye called Methylene Blue (MB) by a Fenton-like reaction. MB has been widely used for coloring paper, temporary hair dyes, dyeing cotton, wools, and as a coating for paper stock and other applications. Their results demonstrated that Fe_3O_4–MWCNT magnetic nanocomposites could effectively adsorb and degrade MB in the presence of H_2O_2 in a wide pH range of 1.0 to 10.0. In addition, the samples presented a high magnetic sensitivity under an external magnetic field, providing an easy and efficient way for the separation of the catalysts from the aqueous solution.

Rueda-Márquez et. al. [52] published a paper involving a sequence of techniques for the treatment of wastewater. Their paper was focused in a multi-barrier treatment (MBT), beginning with a microfiltration membrane pretreatment (MF), followed by hydrogen peroxide photolysis (H_2O_2/UVC) and finishing with CWPO using granular activated carbon (GAC).

Table 3 shows related studies on CWPO.

Ribeiro et al. [1] reported CWPO experiments in the presence of an alternating (AC) magnetic field, using a cobalt ferrite core in a graphitic shell as a catalyst for the mineralization of a simulated pollutant solution containing 4-nitrophenol. As a result, high mineralization was obtained (79%) after 4 hours of reaction.

Munoz et al. [21] tested alumina (Al_2O_3) due to its mechanical, electrical and chemical stability as catalyst support for Fe_2O_3 and Fe_3O_4. The activity and stability of the catalysts were analyzed in 4-chlorophenol, 2,4-dichlorophenol and 2,4,6-trichlorophenol. The results showed complete dechlorination of all chlorophenols tested with mineralization above 70% after 4 hours of reaction time.

Sun et. al. [56] studied the degradation of two emerging pollutants, carbamazepine (CBZ) and ibuprofen (IBP), with nano-magnetite as catalyst. Under the ideal conditions found by the authors, they performed the conversion of CBZ and IBP, reaching values of 86 and 83%, respectively.

Silva et. al. [59] worked on the treatment of paracetamol (PCM) using natural clay-based materials as catalysts, which were produced using an acid-activated treatment, calcination and pillarization with Fe and Co. After 6 hours of reaction, all PCM was removed and insignificant leaching of iron (less than 0.1 $mg \cdot L^{-1}$) was observed.

Velichkova et. al. [60] evaluated the activity of nanostructured magnetite and maghemite catalysts (6 $g \cdot L^{-1}$) in the oxidation of PCM. Some of the results showed that PCM mineralization was improved at high temperature. They achieved 50% of mineralization using nanostructured magnetite as catalyst. All iron oxides exhibited low iron leaching of less than 1%.

Table 3. Summary of some of the related studies devoted to the CWPO process.

Catalyst	T (°C)	Pollutant	[Pollutant]	pH	Reference
$CoFe_2O_4$/MGNC	24	4-nitrophenol	5 $g \cdot L^{-1}$	3	Ribeiro et. al.[1] (2019)

Table 3. Summary of some of the related studies devoted to the CWPO process.

Catalyst	T (°C)	Pollutant	[Pollutant]	pH	Reference
Fe_3O_4/γ-Al_2O_3 Fe_2O_3/γ-Al_2O_3	50	4-chlorophenol 2,4-dichlorophenol 2,4,6-trichlorophenol	100 mg·L^{-1}	3	Munoz et al.[21] (2015)
nano-Fe_3O_4	23	Carbmazepine Ibuprofen	15 mg·L^{-1}	7	Sun et al.[56] (2013)
Fe/Co-Pillared Clay	80	Paracetamol	100 mg·L^{-1}	3.5	Silva et al.[59] (2019)
Nanostructured magnetite and maghemite	60	Paracetamol	100 mg·L^{-1}	2.6	Velichkova et al.[60] (2013)

Paracetamol (acetaminophen or 4-acetylaminophene-nol) is extensively used as a pain reliever and reducing fever. Among contaminants of emerging concern across the European Union, paracetamol deserves special attention because it has been found as a potential pollutant of waters and it's not completely removed from wastewater by the wastewater treatment plant (WWTP) [59,61–63]. Therefore, this work seeks to transform paracetamol in more bio-degradable forms such as CO_2 and H_2O from the CWPO reactions.

Thus, the hybrid cobalt ferrite NPs can be synthesized to act as catalysts in the CWPO process, from the synthesis of the core by the sol-gel method [3] up to the coating process [8]. This process promotes the total degradation of paracetamol, high levels of mineralization, low iron leaching and easy separation of the catalyst from the media through a magnetic field. As seen in Table 3, there are works regarding the use of $CoFe_2O_4$ as catalyst in CWPO. However, just a few researchers tested this catalyst for the treatment of the pollutant PCM with the interest to investigate the oxidation reactions involved in the process through kinetic modeling.

Chapter 3: Methodology

3 METHODOLOGY

3.1 Materials

For the synthesis of the magnetic core, iron (III) chloride hexahydrate (99%, Merck) and cobalt (II) chloride hexahydrate (99%, Fisher Chemical) were used. The solvents used in the sol-gel reaction of the core were ethylene glycol (99.5%, Fluka Analytical) and ethanol absolute (99.8%, Fisher Scientific). Ammonium hydroxide solution (28%, Applichem-Panreac) was used to enable the coprecipitation of the nanoparticles. In the early stages of the coating reaction, the hybrid cobalt ferrite/carbon was dispersed in ethanol absolute (99.8%, Fisher Scientific) and distilled water. The hydrolysis and polymerization of TEOS (98%, Fluka) was favored in this stage of the process. Subsequently, as the reaction progressed, and the TEOS hydrolysis and polymerization processes neared completion, the polymerization of resorcinol (99%, Fisher Scientific) and formaldehyde (37-38% p/p, Panreac) became the predominant process, resulting in the formation of a phenolic resin polymer. To remove the silica, sodium hydroxide (99.1%, Fisher Scientific) was used.

The CWPO runs were performed using paracetamol (98%, Alfa Aesar), hydrogen peroxide (30% w/v, Fisher Chemical), sulfuric acid (98%, Panreac), ultrapure water, ortho-phosphoric acid (85%, Riedel-de Haen), hydroquinone (99% Merck), 4-benzoquinone (99%, Acros Organics), resorcinol (99%, Fisher Scientific), 2-nitrophenol (98%, Aldrich Chemistry), 2-nitroresorcinol (98%, Alfa Aesar) 4-nitrocatechol (≥ 98%, Fluka) and pyrocatechol (99%, Fluka).

3.2 Process Flowchart

For a better understanding of the process studied in this work, since the synthesis of the catalysts until their application in CWPO, the flowchart shown in Figure 8 represents the steps of the methodology used.

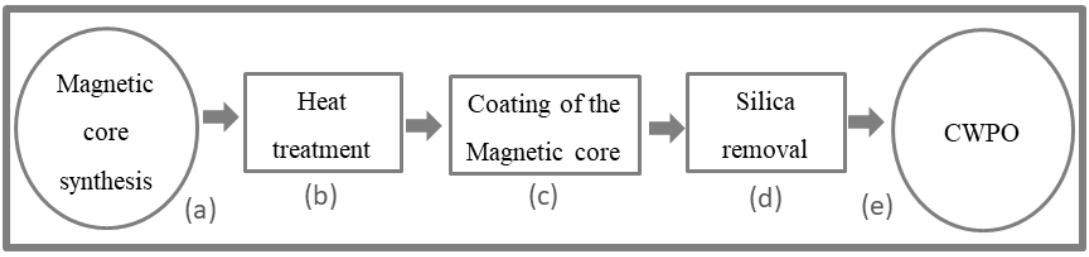

Figure 8. Flowchart of the process

a) Synthesis of the magnetic core;
b) Heat treatment;
c) Coating and carbonization under a N_2 atmosphere;
d) Silica removal (etching);
e) CWPO of paracetamol.

3.3 Preparation of the catalysts

3.3.1 Synthesis of the Magnetic Core

The magnetic core was synthesized according to the methodology described by Giannakopoulou et. al. [3], using a solution of Fe (III) and Co (II) with a 1:2 molar ratio of $CoCl_2.6H_2O$ and $FeCl_3.6H_2O$. The solvents used were 10 mL of ethyl alcohol and 40 mL of ethylene glycol.

The $CoCl_2.6H_2O$ (2.38 g) was weighed and dissolved in ethyl alcohol. This solution was heated with a magnetic stirring plate with a temperature control (IKA® C-MAG HS 7, Figure I – Annex A), until reaching the boiling point at 78 °C. The cobalt solution was then cooled in an ice bath until thermal equilibrium was reached. The $FeCl_3.6H_2O$ (5.41 g) was then weighed and dissolved in ethylene glycol. This solution was heated with a magnetic stirring plate for 5 minutes at 60 °C. Soon after, the iron solution was cooled in an ice bath until thermal equilibrium was reached.

When both solutions achieved 25 °C, they were transferred to a single beaker. The temperature of 25 °C was stipulated to be the initial temperature of the synthesis. The final red-brown solution was warmed up to 60 °C for 2 h in a round bottom flask under a magnetic stirring plate. Finally, it was dried at 189 °C in the same round bottom flask, until it became a gel and then a solid. A representation of this synthesis methodology can be observed in Figure 10.

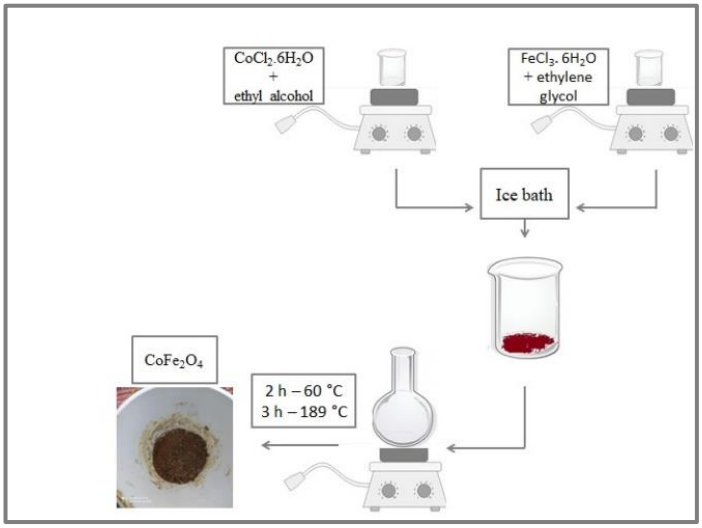

Figure 9. Magnetic core synthesis methodology

Finally, it was transferred to a crucible and the powder was heat-treated in a muffle (Figure II - Annex A) at 300 °C for 24 h and then at 600 °C for 12 h under ambient atmosphere where crystallization to cobalt ferrite took place.

3.3.2 Carbon coating of the Magnetic Core

The process of carbon coating of the magnetic nanoparticles is illustrated in Figure 11.

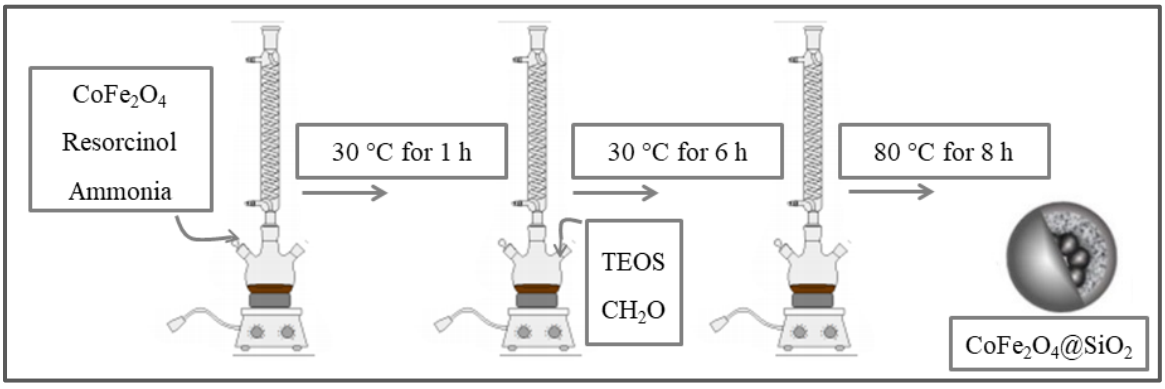

Figure 10. Coating process of the magnetic nanoparticles

The protocol proposed by Rodrigues et. al. [8] was used to produce the carbon-based coating. In a first step, 0.25 g of magnetic nanoparticles synthesized by the method previously described were measured and placed into a 250 mL Erlenmeyer flask containing 150 mL of absolute ethanol and 50 mL of distilled water. The solution was placed in an ultrasonic bath, Ultrasons-H, P- Selecta (Figure III - Annex A), at room temperature until all the magnetite particles were dispersed in the medium for 1 h. The

dispersion was transferred to a 500 mL round bottom flask, which contained 0.1 g of resorcinol and 1.2 mL of a 28% ammonia solution. The flask was placed in an oil bath and stirred with a magnetic stirrer at 30 °C for 1 h. Subsequently, 210 µL of TEOS and 150 µL of formaldehyde (37 – 40%) were added dropwise and stirred for 6 h at 30 °C. Subsequently, the temperature was raised to 80 °C and the round bottom flask remained at this temperature for 8 h. The magnetic product resulting from this protocol, denoted as $CoFe_2O_4@SiO_2$, was washed using deionized water until neutral pH, the water separated using a centrifuge (6000 rpm for 5 min) and then washed again with absolute ethanol. The resulting material was then dried overnight at 60 °C and subsequently weighted and stored in a vial.

In a second step of the coating process, the polymer-coated nanoparticles were carbonized under a N_2 atmosphere in a vertical tubular furnace (ROS 50/250/12, Thermoconcept, Figure IV - Annex A). The gas phase thermal treatment was conducted under a N_2 flow (100 $cm^3 \cdot min^{-1}$) at 120 and 400 °C during 1 h at each temperature and then at 600 °C for 4 h, with an heating ramp of 2 $°C \cdot min^{-1}$. The resultant carbon-coated magnetic nanoparticles were denoted as $CoFe_2O_4@SiO_2@C$.

3.3.3 Removal of silica by etching process

The $CoFe_2O_4@SiO_2@C$ nanoparticles were etched via stirring with a sodium hydroxide solution 10 M. For that purpose, 10 mg of nanoparticles were added to 1 mL of the NaOH solution in an Erlenmeyer and left under vigorous magnetic stirring for 16 h. The resulting material was washed with distilled water untl neutral pH using a centrifuge (6000 rpm for 5 min) and then washed with absolute ethanol. The material was dried overnight at 60 ºC in a drying chamber, resulting in the carbon-based magnetic nanoparticles (GbMNPs) with a yolk-shell nanostructure, denoted as $CoFe_2O_4@void@C$.

3.4 CWPO of paracetamol

3.4.1 Reaction System

The batch oxidation runs were performed adapting the methodology reported by Silva et. al. [59]. The stoichiometric amount of hydrogen peroxide needed for the complete mineralization of paracetamol, according to the chemical reaction given by Eq. 9.

$$C_8H_9NO_2 + 21H_2O_2 \rightarrow 8CO_2 + HNO_3 + 25H_2O \quad (9)$$

Considering 100 mL of a paracetamol solution with concentration of 100 $mg \cdot L^{-1}$, the amount of hydrogen peroxide necessary to proceed with the experiment is 158 µL of a 30%w/v peroxide solution. The oxidation reactions were carried out in a 500 mL round-bottom flask reactor with a magnetic stirring plate (600 rpm), equipped with a condenser and a controller to measure the temperature. The reactor was loaded with 100 mL of a 100 $mg \cdot L^{-1}$ paracetamol solution to simulate hospital water effluents. It was previously acidified until pH 3.5 employing H_2SO_4 (1M). The paracetamol concentration and the pH were stipulated so that the degradation of PCM could be clearly shown in the analysis of HPLC[59]. The reactor, Figure 11, was heated by immersion in an oil bath monitored by the temperature controller until 80 °C.

Figure 11. The reaction system used in the CWPO runs

When temperature stabilized, the described amount of hydrogen peroxide was added to the reactor. After the complete mixing of the reactants, 0.25 g of catalyst was added into the reactor. This moment was considered as the beginning of the CWPO run (t = 0).

Samples for analysis were periodically withdrawn at selected times: 5, 15, 30, 60, 120, 240, 360, 480 and 1440 min. At each time, 3 samples of 1 mL were collected and stored in different Eppendorf tubes, previously prepared according to the analysis that would be done, as determination of H_2O_2 concentration, paracetamol concentration and TOC. To stop the oxidation reactions at the time of sample collection, approximately 10

mg of Na_2SO_3 was placed in the Eppendorfs for the paracetamol and TOC analysis. The sodium sulfite reacted with the peroxide stopping the formation of hidroxyl radicals and, consequently, the oxidation reactions. We did not add Na_2SO_3 in the Eppendorfs for the hydrogen peroxide analysis since our objective is to study the amount of H_2O_2 was consumed in a determined time of reaction. Each sample was separated by a magnetic field and the liquid aliquot was reserved for the analysis. After the last sample withdrawal, the catalyst was separated by a magnetic field and the liquid media stored in a refrigerator for later analysis by atomic absorption. Finally, the catalyst was washed with distilled water and dried overnight in an air oven at 50 °C.

A non-catalytic run was conducted in the same conditions as the CWPO run, but in the absence of catalyst.

3.4.2 Analytical Methods

The quantification of hydrogen peroxide was performed by a colorimetric method, adapting the methodology reported by Masso [64]. To monitor the decomposition of H_2O_2 it was necessary to obtain a calibration curve in the concentration range from 0 to 220 $mg \cdot L^{-1}$. For that, 1 mL of different concentration solutions of H_2O_2 was added in a 20 mL volumetric flask with the solution of H_2SO_4 (1 mL/0.5 M) and $TiOSO_4$ (0.1 mL) and then diluted again with distilled water. Then, the samples were analyzed by UV-Vis spectrophotometry (T70 spectrometer, Figure V - Annex A) at a wavelength of 405 nm to determine its absorbance. Figure 12 shows the calibration curve obtained.

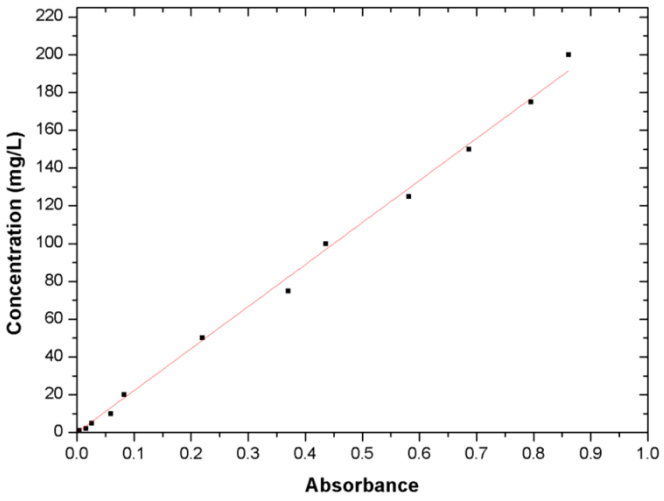

Figure 12. Calibration curve for determination of H_2O_2 concentration

The value of R^2 is 0.997 and 9 points of calibration show a good adjustment.

HPLC measurements were performed with a Jasco HPLC system equipped with a UV-vis detector (UV-2075 Plus), a quaternary gradient pump (PU-2089 Plus) for solvent delivery (0.65 mL·min^{-1}) and a RES ELUT 5 µ C18-90 Å column (150 mm x 4.6 mm) of VARIAN (Figure VI – Annex A). With this methodology, it was possible to analyze the model pollutant, paracetamol, and its possible oxidized intermediates, such as hydroquinone, catechol, *p*-benzoquinone, *p*-aminophenol and *4*-nitrophenol. The wavelength used to measure the absorbance of these compounds was 277 nm. For the oxidized intermediates, namely 2-nitrophenol, 2-nitroresorcinol, resorcinol, 4-nitrophenol, hydroquinone, pyrocatechol and phenol, the wavelength was 244 nm.

For the quantification of TOC, 1 mL of the samples taken from CWPO was diluted in a 20 mL volumetric flask and then analyzed in the equipment SHIMADZU TOC-L (Figure VII – Annex A).

The quantification of iron in the remaining solutions after the CWPO runs was performed to determine the leached iron from both materials, $CoFe_2O_4$ and $CoFe_2O_4$@void@C, to the reaction media. The amount of iron in the samples was determined by atomic absorption, using the equipment Spectra Varian equipped with a Varian hollow cathode lamp at a wavelength of 248.3 nm. The first step was to obtain the calibration curve, Figure 13, in the range of 0.06 – 2 mg·L^{-1}.

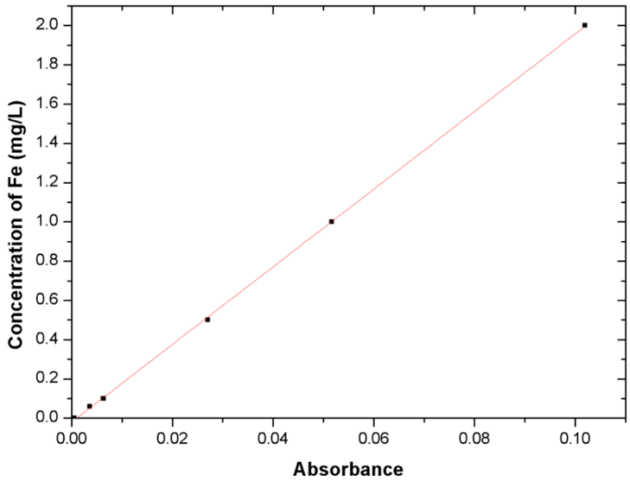

Figure 13. Calibration curve for the measurement of iron leached

The value of R^2 was found to be 0.999, which shows a good fit for the linear regression. The effluents from the CWPO runs were filtered in a 45 µm membrane and

the supernatant was stored in a vial and then analyzed in the equipment, to obtain its absorbance and consequently the iron concentration.

3.5 Adsorption of paracetamol

For the paracetamol adsorption runs, 100 mL of the same paracetamol solution used in the CWPO runs (100 $mg \cdot L^{-1}$) was added in a 500 mL round-bottom flask loaded with 0.25 g of the adsorbent (2.5 $g \cdot L^{-1}$ of concentration). The adsorption run was carried out in a magnetic stirring plate (600 rpm) for 24 h at 80 °C, equipped with a condenser and a controller to measure/control the temperature. Afterward, the suspension was separated magnetically, and the remaining liquid was analyzed by HPLC to determine the concentration of paracetamol. The amount of paracetamol adsorbed was calculated by the difference between the initial and the final concentration.

3.6 Characterization Techniques

Structural characterization and average crystallite size were measured by X-ray Diffraction (XRD) using Cu-K_α radiation ($\lambda = 0.15$ nm) in a Bruker D8 Discover diffractometer (Figure VIII – Annex A) operating in the Bragg-Brentano geometry. The data were collected at room temperature in the 2θ range 5° - 80° at a step of 0.05°. To identify the phase composition of the samples, structural data from the International Centre for Diffraction Data (ICDD) was used. The mean crystallite sizes of the samples were calculated based on the spinel structures of the $CoFe_2O_4$ nanocrystals by applying peak broadening of the (311) peak using Scherrer's formula as seen in Eq. 10.

$$D = \frac{0.9\,\lambda}{\beta_d \cos\theta} \tag{10}$$

where D is the mean crystallite size, λ is the wavelength of the Cu-K_α radiation (λ = 0.154 nm), β_d is the full width at half maximum (FWHM) in radians and θ is the correspondent Bragg diffraction angle in radians.

To compare the results, another method to analyze the size of the nanomaterials was conducted. While Scherrer's formula considers only the effect of crystallite size on the XRD peak broadening, the Williamson-Hall (W-H) method is based on a physical line broadening of X-ray diffraction peaks occurring due to the size and micro-strain of the

nanocrystals [65]. Thus, the W-H method takes into consideration the micro-structures of the lattice about the intrinsic strain, which gets developed in the nanocrystals due to the point defect, grain boundary, triple junction, and stacking faults [66,67,68]. The total broadening can be written as in Eq. 11.

$$\beta_{total} = \beta_{size} + \beta_{strain} \quad (11)$$

The Uniform Deformation Model (UDM) considers a uniform strain deformation throughout the crystallographic direction, which is introduced in the nanocrystals due to crystallographic imperfections [66]. The intrinsic strain actually affects the physical broadening of the XRD profile and this expansion of the strain-induced peak can be expressed as in Eq. 12.

$$\beta_{strain} = 4\,\varepsilon.tan\theta \quad (12)$$

Hence, the total broadening due to strain and size at a particular peak having the diffraction plane directions hkl, can be expressed as in Eq 13.

$$\beta_{hkl} = \beta_{size} + \beta_{strain} \quad (13)$$

where β_{hkl} is the full width at half of the maximum intensity for different diffraction planes. Re-arranging Equation 10 to 13, Eq. 14 is obtained.

$$\beta_{hkl}.cos\theta = \frac{0.9\,\lambda}{D} + 4\,\varepsilon.sin\theta \quad (14)$$

To obtain the crystallite size, it's necessary to plot $\beta_{hkl}.cos\theta$ (Y-axis) as a function of $4sin\theta$ (X-axis) and, after obtaining a regression equation that described the data with the independent term, it is possible to calculate D.

Transmission Electron Microscopy (TEM) was performed in an H-9000 instrument operating at 300 kV. ImageJ software (NIH, Bethesda, MD, USA) was used to estimate the size of the magnetic nanoparticles.

The Fourier Transform Infrared Spectroscopy (FTIR) spectra of the $CoFe_2O_4$@void@C sample were recorded on a Perkin Elmer FT-IR spectrophotometer UATR two infrared spectrophotometer, with a resolution of 4 cm^{-1}. The range of wavenumber used in the analysis was from 450 to 4000 cm^{-1}. All the measurements were done from the solid samples at room temperature.

Chapter 4: Results and discussion

4 Results and discussion

4.1 Characterization of materials

4.1.1 X-ray Diffraction (XRD)

Figure 14 shows the XRD patterns of the core $CoFe_2O_4$ powders prepared by the sol-gel method and of the $CoFe_2O_4$@void@C. As it can be observed, the diffraction peaks of the XRD pattern can be indexed to $CoFe_2O_4$ cubic spinel structures with space group Fd-3m (JCPDS Card No 00-001-1121). After coating, the catalyst structure remained the same, as shown by the characteristic peaks.

The peaks at 18°, 30°, 35°, 37°, 43°, 53°, 57°, and 62° are attributed to the crystal planes of the cobalt ferrite cores at 111, 220, 311, 222, 400, 422, 511, and 440 respectively.

It is perceived that the peaks at 18°, 57°, and 62° in the XRD pattern of the $CoFe_2O_4$@void@C sample increases significantly. There are several studies about the improvement of calcination processes in the synthesis of nanoparticles to achieve materials with a high degree of crystallinity and no impurities [11,3,69]. Some of the calcination methods reported the increase of the temperature and time of exposure to obtain more crystallinity. To avoid impurities, the use of an inert atmosphere provided a route to purify the nanostructure [70,71]. Since the peaks of the diffractogram in Figure 15 (b) became sharper and well-defined, although the same as in the diffractogram of the uncoated ferrite, it is suggested that the coating process favored the development of the material, taking into account the longer time of heat treatment in the tubular furnace at 400 and 600 °C necessary to synthesize the yolk-shell shape, as well as the N_2 atmosphere that the nanomaterial was exposed.

In particular, the crystallite size of the prepared $CoFe_2O_4$ powders is 47 nm, as calculated by the Scherrer equation from the (311) peak. Using the W-H method the crystallite size is 53 nm.

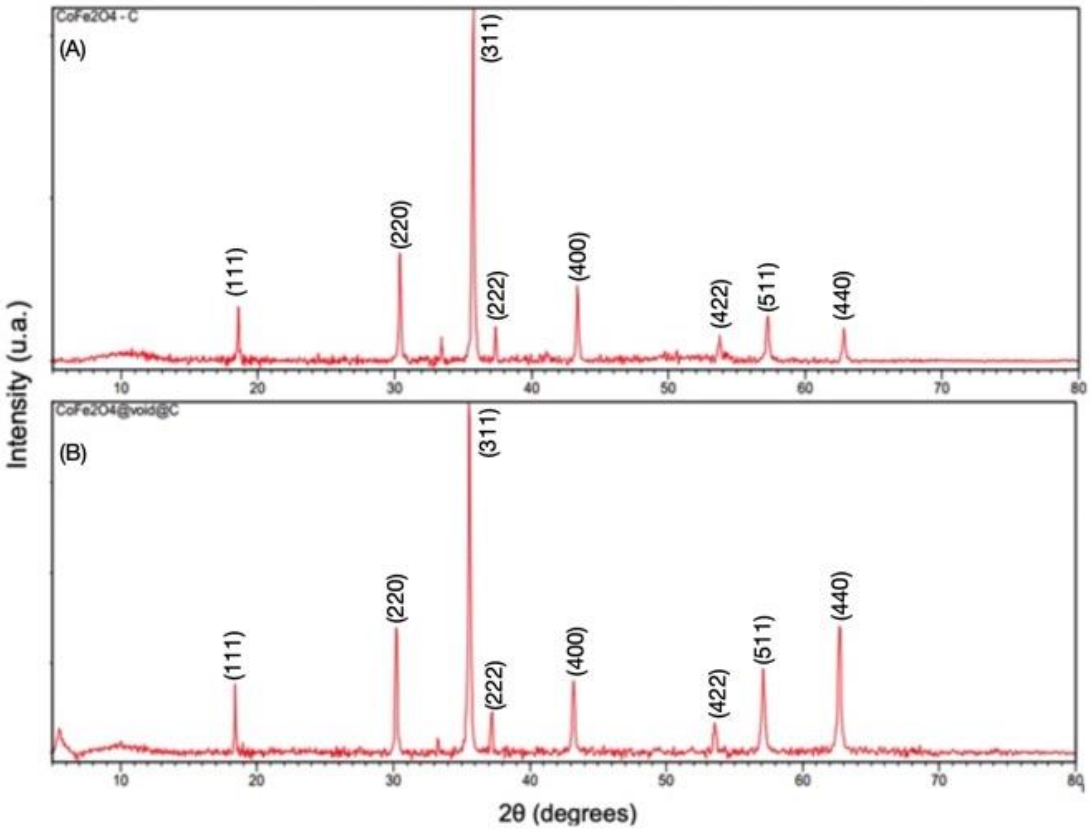

Figure 14. XRD diffractograms of the (a) core $CoFe_2O_4$ and of the (b) $CoFe_2O_4$@void@C

The crystallite size calculated for the core $CoFe_2O_4$ is according to the size of magnetic nanoparticles reviewed in the literature. Giannakopoulou et al. [3] reported that the sol-gel synthesis of $NiFe_2O_4$ nanoparticles observed an increase in particle size and crystallinity with the increase of the annealing temperature. The crystal sizes of the nanoparticles annealed at 600 and 900 °C correspond to 20 and 50 nm, respectively. Pottker et al. [11] prepared $NiFe_2O_4$ nanoparticles by the co-precipitation method subjected to calcination at temperatures of 700, 800, 900, and 1000 °C for 120 min at atmospheric pressure. No characteristic peaks of impurities were observed in the samples. The crystallite size was calculated from peak 311 using Scherrer's equation varies from 7.4 to 30.1 nm, as a function of the calcination temperature. Hussain et al. [72] created a system of $Ni_{1-x}Mn_xFe_2O_4$ with x = 0.0 to 0.9 prepared by sol-gel auto combustion technique using chlorides of Ni, Mn, and Fe. Further heat treatment for 5 h at 500 °C was needed to enhance the crystallinity. The structure was a single-phase, face-centered cubic with particle size in the range of 23.86 to 38.30 nm, depending on the composition x. Hashemi et al. [33] conducted a study about the synthesis of $CoFe_2O_4$ nanoparticles by a sol-gel auto-combustion method in the simultaneous presence of ethylene glycol and agarose as

complexing agents and nitrates as precursors. The samples with the equivalence ratio Chemical reagents/Nitrates of 1 and 2 obtained a crystallite size of 28 ± 3 and 24 ± 0.5 nm respectively.

4.1.2 Transmission Electron Microscopy (TEM)

The TEM image presented in Figure 15(a) shows the bare cobalt ferrite core synthesized through the sol-gel method in this work with an average size of 53.51 ± 4.2 nm, determined using the ImageJ software. It almost equals the value obtained by the W-H method from the XRD spectrum. The observed agglomeration is related to the ferromagnetic characteristics of the sample. By the shape and morphologies of $CoFe_2O_4$@void@C observed in Figure 15(b), the lighted shadowy border evidences the coating of the magnetic nanoparticles and the cobalt ferrite core shelled by a carbon-based layer, as observed elsewhere [42,1]. As expected, the increment of the number of carbon-based precursors (resorcinol, formaldehyde, and TEOS) in relation to a fixed mass of the magnetic core provided an increase of the carbon-based shell thickness, which resulted in particles with average sizes of 59 ± 8.1 nm.

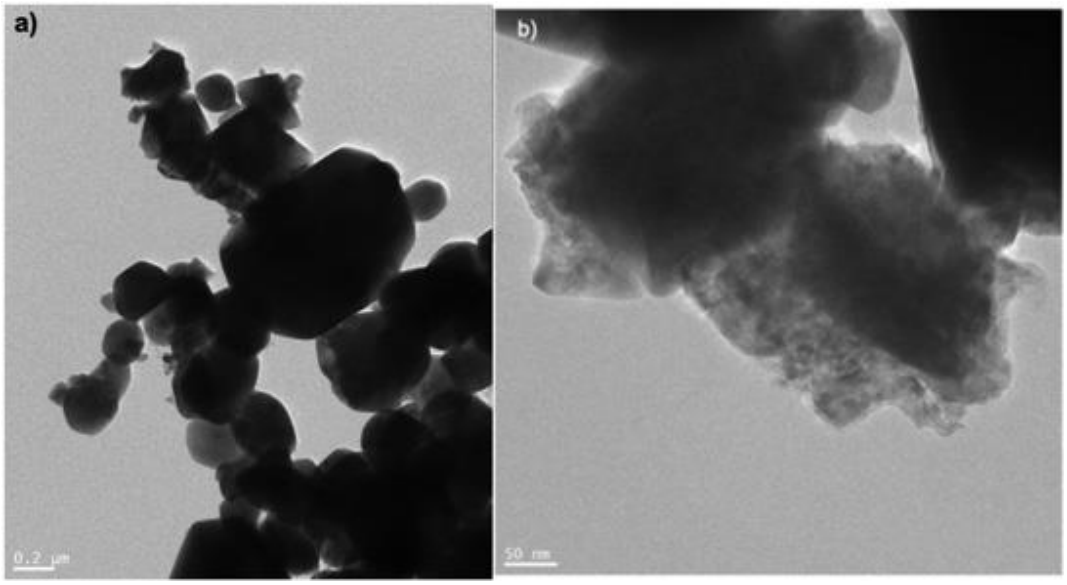

Figure 15. TEM image of the: (a) Magnetic core ($CoFe_2O_4$); (b) $CoFe_2O_4$@void@C

The work reported by Ribeiro et al. [1] about the preparation of magnetite, nickel, and cobalt ferrites encapsulated within graphitic shells shows similar results. The core-shell structures of $NiFe_2O_4$/MGNC and $CoFe_2O_4$/MGNC had a crystallite size of 33 ± 5 and 33 ± 2 nm, respectively. The average size of the nickel and cobalt ferrites is 36 ± 15

and 56 ± 18 nm, respectively determined from TEM measurements. Desai et al. [74] reported a study regarding the Zn-Zr co-substitutes cobalt ferrite nanoparticles ($CoZn_xZr_xFe_{2-2x}O_4$, x = 0 – 0.4) synthesized by sol-gel auto-combustion route. The formation of the cubic phase of $CoFe_2O_4$ was revealed by X-ray. The particle size was measured by TEM, being the values for the samples with x = 0.2 and 0.4 of 45 and 80 nm, respectively. Lunhong and Jiang [75] prepared cobalt ferrite NPs by a one-step sol-gel auto-combustion method. It was found that the particle size and magnetic properties of the samples showed a strong dependence to the annealing temperature. The samples heat-treated at 700 °C seem as quasi-spheres with the crystallite size in the range of 25 - 30 nm.

4.1.3 Fourier Transform Infra-Red spectroscopy (FTIR)

Figure 16 shows the FTIR spectra of $CoFe_2O_4$@void@C recorded between 4000 and 550 cm^{-1}.

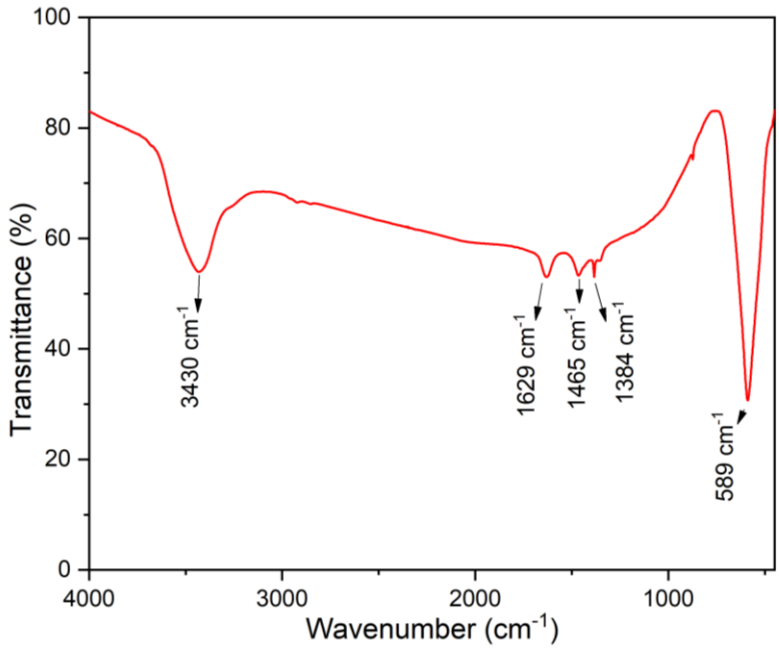

Figure 16. FTIR spectra of the $CoFe_2O_4$@void@C nanoparticles

The bands were compared and analyzed according to the literature of cobalt ferrite materials [76,77,78]. The FTIR spectra of the hybrid coated ferrite showed a strong band at 589 cm^{-1}, which confirms the metal oxide bands in the spinel structure due to the stretching vibrations of metal oxide in the octahedral group complex Co(II)-O^{2-} or in the

Fe(III)-O^{2-} tetrahedral group complex of the cobalt ferrite phase. The band observed at 3430 cm^{-1} is attributed to the O-H stretching vibrations and the absorption band present at 1629 cm^{-1} is due to the bending of the absorbed water molecules. Meanwhile, the band at 1465 cm^{-1} is due to the symmetric C-H stretching vibrations. The band at 1020 cm^{-1} may be attributed to C-O-C stretching.

4.2 Catalytic Wet Peroxide Oxidation (CWPO)

In order, to evaluate the efficiency of the $CoFe_2O_4$ magnetic core and of the $CoFe_2O_4$@void@C, the concentrations of PCM, H_2O_2, and TOC were followed during the reaction time. To confirm the activity of the catalysts, a non-catalytic run in the same conditions was performed. Figure 17 shows the concentrations of H_2O_2, PCM, and TOC as a function of time of reaction.

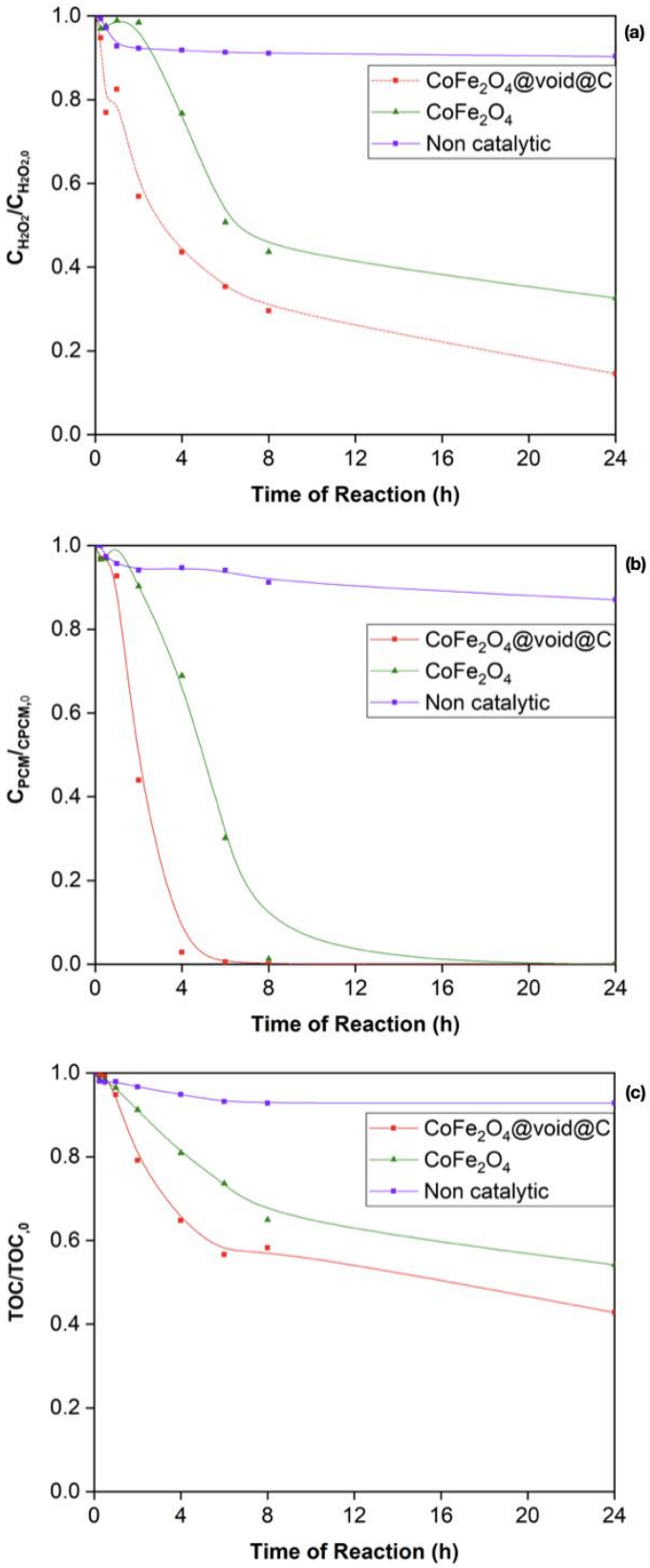

Figure 17. Normalized concentrations of (a) H_2O_2, (b) PCM and (c) TOC upon reaction time, under the following operational conditions: $C_{PCM,0}$ = 100 mg·L^{-1}, $C_{H_2O_2,0}$ = 472.4 mg·L^{-1}, C_{cat} = 2.5 g·L^{-1}, pH_0 = 3.5 and T = 80 °C

As observed, both materials are active in the CWPO of PCM. The decomposition of H_2O_2, shown in Figure 17(a), achieved values of 10, 68, and 85% at 24 h of reaction time for the non-catalytic run, and for the runs with the catalysts $CoFe_2O_4$ and $CoFe_2O_4$@void@C, respectively.

Regarding the conversion of PCM, Figure 17(b) reveals that the best-tested material is $CoFe_2O_4$@void@C, showing 99.5% of conversion after 6 h of reaction. The uncoated ferrite after the same time of reaction achieved 70% of PCM conversion, while in the non-catalytic run only 6% was obtained.

As it can be observed in Figure 17(c), the materials showed higher conversions of TOC, agreeing with the results obtained so far for conversions of paracetamol and H_2O_2. The core $CoFe_2O_4$ and the $CoFe_2O_4$@void@C achieved mineralization values of 46 and 58% respectively after 24h of reaction time.

The best performance when employing the $CoFe_2O_4$@void@C as a catalyst compared with the uncoated ferrite is conducive since the peaks in the XRD pattern of the $CoFe_2O_4$@void@C sample increases significantly when compared to the $CoFe_2O_4$. This indicates that the hybrid coated ferrite achieved a higher degree of crystallinity. The $CoFe_2O_4$@void@C has also a higher surface area, which also leads to superior catalysis.

There are works regarding the degradation of paracetamol by CWPO [1,59], oxidation by ozonation with H_2O_2/UV [79], and heterogeneous Fenton-like process [60]. Silva et. al. [59], under the same conditions as those used in this study, also obtained a conversion of 90% of paracetamol after 4 h of reaction, but the complete conversion only occurred after 6 h. Najjar et. al. [79] used the oxidation by ozonation and H_2O_2/UV processes for the removal of paracetamol, with the initial concentration of the pollutant of 100 $mg \cdot L^{-1}$ and a concentration of H_2O_2 of 1,700 $mg \cdot L^{-1}$ during 90 minutes of time reaction. However, the amount of hydrogen peroxide used by Najjar et. al. was 360% higher than the stoichiometric concentration necessary to degrade the pollutant, which is not favorable when thinking on cost and safety issues that excess of hydrogen peroxide may bring into consideration. Velichkova et. al. [60] reported a heterogeneous Fenton-like process to treat paracetamol using iron oxides nano and submicro magnetite as a catalyst. The initial concentration of pollutant was the same used in this work, and a higher initial concentration of the catalyst equals to 6 $g \cdot L^{-1}$. The authors achieved the complete conversion of the paracetamol within 5 h of reaction.

In previous studies that analyzed the removal of TOC in the CWPO of paracetamol [60,62,59], the mineralization values reported in our work at the end of the process were not achieved. For example, in the work done by Velichkova et. al. [60], the highest mineralization achieved with the best material was 43% after 5 h of reaction.

Figure 18 depicts the liquids recovered after the CWPO runs with both catalysts (the uncoated and the hybrid coated ferrite).

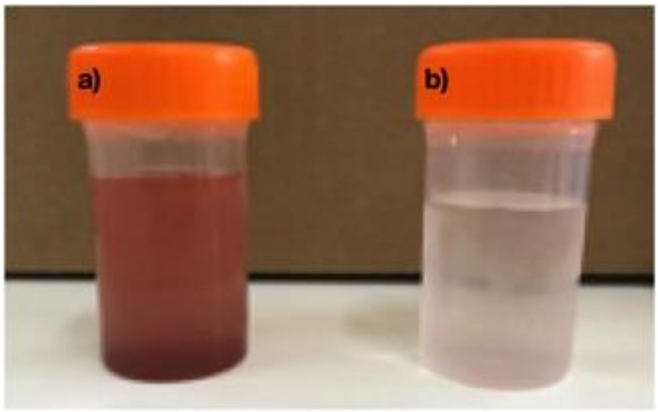

Figure 18. Reaction medium recovered after the CWPO, upon removal of the catalysts (a) $CoFe_2O_4$ and (b) $CoFe_2O_4$@void@C, respectively

The determination of iron leached from the catalysts for the reaction solution was done for each PCM CWPO run after 24 h of reaction. As expected, the $CoFe_2O_4$@void@C material with the carbon-coated achieved a better result (iron leaching of 1.59 $mg \cdot L^{-1}$) when compared to the uncoated ferrite which had an iron leaching to the solution of 2.54 $mg \cdot L^{-1}$. The information about the percentage of iron leached also indicates that the hybrid coated ferrite is a more stable catalyst and that the amount of iron at the end of the reaction run is within the limit concentration of 2 $mg \cdot L^{-1}$ of iron in water, as established by law.

The conversions of paracetamol and TOC, and the efficiency of H_2O_2 consumption at 6 h of reaction, are represented in Figure 19. The efficiency of H_2O_2 (η_{H2O2}) was determined according to Eqs. 15, 16, and 17.

$$x_{H_2O_2} = \frac{C_{H_2O_2,0} - C_{H_2O_2}}{C_{H_2O_2,0}} \quad (15)$$

$$x_{TOC} = \frac{C_{TOC,0} - C_{TOC}}{C_{TOC,0}} \quad (16)$$

$$\eta_{H_2O_2} = \frac{x_{TOC}}{x_{H_2O_2}} \quad (17)$$

Analyzing the results, it is possible to observe that the hybrid coated ferrite has higher conversions and that the paracetamol can be removed more efficiently.

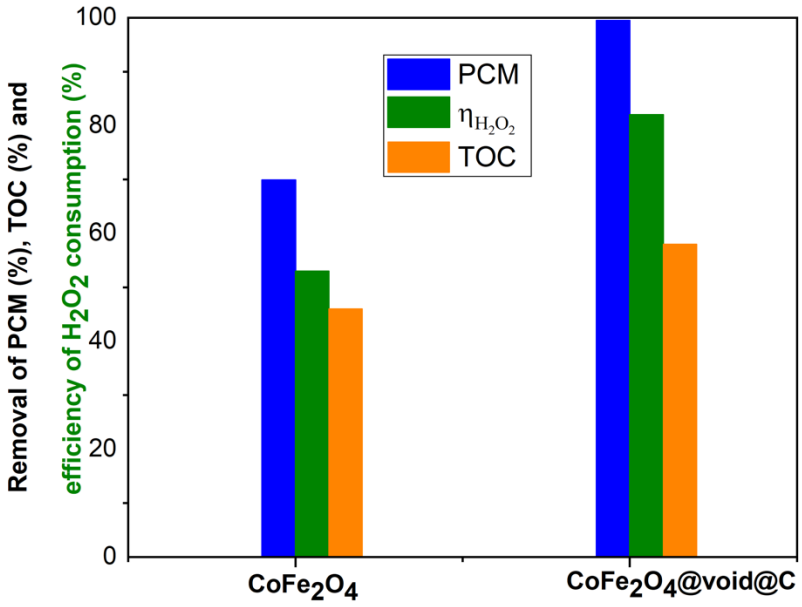

Figure 19. Removal of paracetamol, TOC and efficiency of H_2O_2 consumption at 6 h of reaction, under the following operational conditions: $C_{PCM,0}$ = 100 mg·L^{-1}, $C_{H_2O_2,0}$ = 472.4 mg·L^{-1}, C_{cat} = 2.5 g·L^{-1}, pH_0 = 3.5 and T = 80 °C

To confirm if the removal of the pollutant was occurring by oxidation, rather than by adsorption on the materials, adsorption runs were performed. From the data of the HPLC analysis, the absence of paracetamol adsorption after 24 h was observed.

The hybrid cobalt ferrite/carbon catalyst produced by the sol-gel method described in this work shows high ferromagnetic behavior, even after the CWPO runs, as shown in Figure 20. During the coating process and the CWPO run, it is important to have a magnetic material to provide an abundant recovery of the samples. At the end of the oxidation reactions, it was possible to recover almost 100% of the catalyst using a magnetic field.

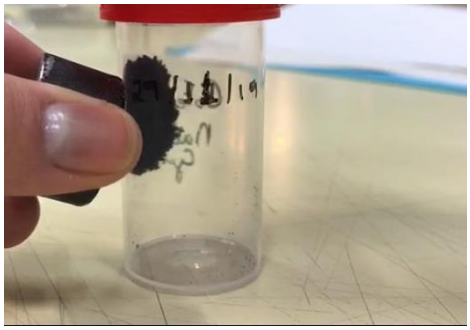

Figure 20. $CoFe_2O_4$@void@C catalysts in the presence of a magnetic field

4.3 Kinetic Modeling

4.3.1 PCM and H_2O_2 disappearance rates

To interpret the role of the oxidation reactions in the CWPO process, the kinetics were modeled from the results shown previously, considering the system as a batch reactor in a constant volume and perfect mixing, where an irreversible reaction occurs and that the composition of the aliquot taken at a given time was identical to the internal composition of the reactor at that time. It was also considered that adsorption was negligible in the whole process.

Different reaction rate equations have been proposed to fit the experimental data, namely first order, pseudo-first order, second order for each species and an autocatalytic-power-law kinetic model developed to predict the observed induction period and the dependence on the consumption of H_2O_2.

Due to lack of monitoring of the oxidation intermediates resulting from the oxidation of the model contaminant, only the rate of disappearance of PCM and H_2O_2 can be defined according to their concentrations, without taking into account the stoichiometry of the multiple reactions that can occur simultaneously, as shown in Eq. 18.

$$C_8H_9NO_2 + H_2O_2 \rightarrow \text{non identified oxidized products} + CO_2 + H_2O \quad (18)$$

The kinetic study was done following the methodology proposed by Diaz de Tuesta et. al. [80–83], in their work dealing with CWPO.

The numerical integration of the rate equations presented in Table 4, with the initial conditions $C_{PCM} = C_{PCM,0}$, $C_{H2O2} = C_{H2O2,0}$ at $t = 0$ was solved by using the software

Python 3.7 (Python Software Foundation, 2020, USA) to minimize the sum of squared errors (SSE) of the relative concentration of each compound *i* ($rc_i = C_i/C_{i,0}$) between the experimental (exp) and predicted (model) values, as given in Eq. 19.

$$SSE = \sum_{n=1}^{N}(rc_{exp\,i,n} - rc_{model\,i,n})^2 \quad (19)$$

The models were also evaluated by the determination factor (R^2) calculated by applying Eq. 20.

$$R^2 = \frac{\sum_{n=1}^{N}(R.C_{model\,i,n} - R.\bar{C}_{model\,i})^2}{\sum_{n=1}^{N}(R.C_{model\,i,n} - R.\bar{C}_{model\,i})^2 + \sum_{n=1}^{N}(R.C_{exp\,i,n} - R.C_{model\,i,n})^2} \quad (20)$$

where N in the total number of values (n) in a run and p is the number of predictors.

Table 4. Kinetic models considered to evaluate the disappearance rates of paracetamol and H_2O_2 in the CWPO run with $CoFe_2O_4$@void@C as catalyst (units in mmol and min).

N°	Kinetic model	Parameters	R^2	*SSE*
1	$\frac{dC_{H_2O_2}}{dt} = -k_{H_2O_2}C_{H_2O_2}$	$k_{H_2O_2}$= 0.0033 min^{-1}	0.95	0.118
2	$\frac{dC_{PCM}}{dt} = -k_{PCM}C_{PCM}$	k_{PCM} = 0.0064 min^{-1}	0.90	0.264
3	$\frac{dC_{H_2O_2}}{dt} = -k_{H_2O_2}C_{H_2O_2}^{\ 2}$	$k_{H_2O_2}$ = 0.00040 L·mmol^{-1}·min^{-1}	0.98	0.033
4	$\frac{dC_{PCM}}{dt} = -k_{PCM}C_{PCM}^{\ 2}$	k_{PCM} = 0.0148 L·mmol^{-1}·min^{-1}	0.67	0.583
5	$\frac{dC_{PCM}}{dt} = -k_{PCM}C_{PCM}(C_0\text{-}C_{PCM})$	k_{PCM} = 0.0627 L·mmol^{-1}·min^{-1} C_0 = 0.6858 mmol·L^{-1}	0.99	0.001

Table 4. Kinetic models considered to evaluate the disappearance rates of paracetamol and H_2O_2 in the CWPO run with $CoFe_2O_4$@void@C as catalyst (units in mmol and min).

N°	Kinetic model	Parameters	R^2	*SSE*
6	$\frac{dC_{H_2O_2}}{dt} = -k_{H_2O_2}C_{H_2O_2}$ $\frac{dC_{PCM}}{dt} = -k_{PCM}C_{PCM}$ $(C_0\text{-}C_{PCM})$	$k_{H2O2} = 0.0033\ min^{-1}$ $k_{PCM} = 0.0624$ $L\cdot mmol^{-1}\cdot min^{-1}$ $C_0 = 0.6855\ mmol\cdot L^{-1}$	0.95	0.063
7	$\frac{dC_{H_2O_2}}{dt} = -k_{H_2O_2}C_{H_2O_2}$ $\frac{dC_{PCM}}{dt} = -k_{PCM}C_{PCM}$ $(C_0\text{-}C_{PCM})C_{H_2O_2}$	$k_{H2O2} = 0.0033\ min^{-1}$ $k_{PCM} = 0.0064\ L^2\cdot(mmol^2)^{-1}\cdot min^{-1}$ $C_0 = 0.6833\ mmol\cdot L^{-1}$	0.94	0.335
8	$\frac{dC_{H_2O_2}}{dt} = -k_{H_2O_2}C_{H_2O_2}^{\ 2}$ $\frac{dC_{PCM}}{dt} = -k_{PCM}C_{PCM}$ $(C_0\text{-}C_{PCM})C_{H_2O_2}$	$k_{H2O2} = 4.1\ 10^{-4}\ L\cdot mmol^{-1}\cdot min^{-1}$ $k_{PCM} = 0.007\ L^2\cdot(mmol^2)^{-1}\cdot min^{-1}$ $C_0 = 0.6832\ mmol\cdot L^{-1}$	0.98	0.252

Figure 21 exhibits the concentrations of H_2O_2 and PCM during the time of reaction. It is observed that the kinetic models of the first and second order for paracetamol did not represent well the experimental data, especially in the case of the second-order model (model N°4).

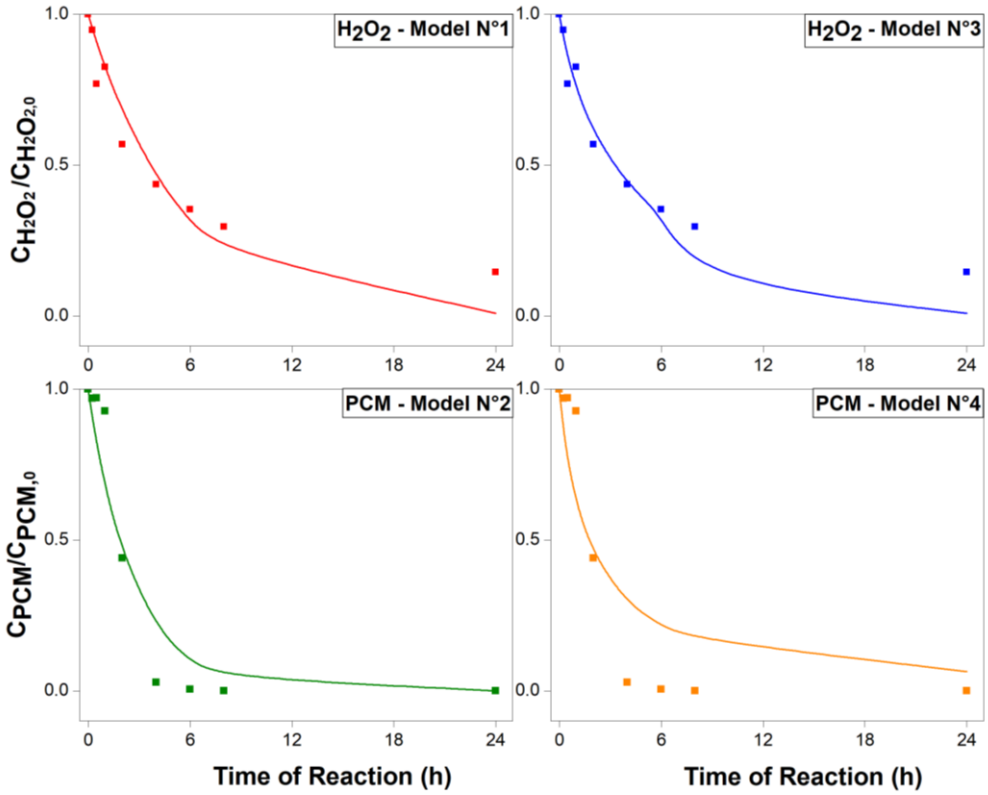

Figure 21. Experimental (symbols) and predicted (lines) concentrations of H_2O_2 (models 1 and 3) and PCM (models 2 and 4)

Regarding the disappearance of H_2O_2, the proposed model N°3 obtained a good representation of the values with a determination factor equal to 0.98.

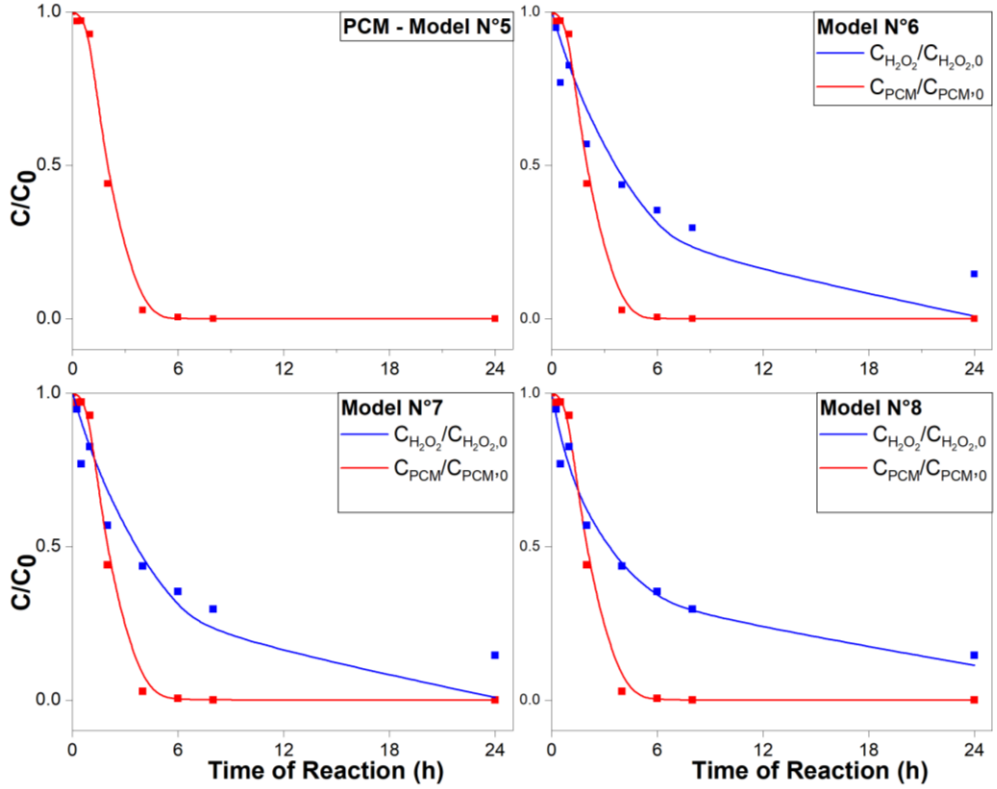

Figure 22. Experimental (symbols) and predicted (lines) concentrations of H_2O_2 and PCM

The initial low-activity period of paracetamol can be well explained by the autocatalytic model, with a determination factor equal to 0.99, model N° 5 (Figure 22). Subsequently, the best models for the pollutants and oxidants were related together and the constant C_0 was determined. It is important to highlight that the value C_0 did not change significantly regardless of the proposed experimental models (0.6858, 0.6855, 0.6833, and 0.6832 mmol·L^{-1} for the models 5, 6, 7, and 8, respectively).

Initially, taking into account that there was no adsorption, as shown in the adsorption run performed, there seems to be an oxidation process occurring at the surface of the catalyst, promoting a higher catalytic activity. As a result of this perceived oxidation, the induction period occurred at the beginning of the reaction. This behavior has been reported in various publications [81,84,48] regarding CWPO with carbon black as a catalyst, suggesting the same in this process as a possible explanation.

Van et al. [85] tested a catalyst derived from iron slag (Fe-S) that was used for heterogeneous Fenton oxidation (H_2O_2/Fe-S) of paracetamol in a range of concentrations between 100 and 500 mg·L^{-1} in an aqueous solution. Kinetic experiments showed that the

degradation of paracetamol occurs better when the concentration of PCM equals 100 $mg \cdot L^{-1}$ and was well fitted with a pseudo-first-order kinetic model. The calculated constant k was 0.0425 min^{-1}. Some of the reasons why the authors achieved such a different value for the kinetic constant is because they reported an adsorption process of paracetamol at the surface of Fe-S, while in this work the adsorption run did not show any adsorption.

Diaz de Tuesta et. al. [82] performed work to understand the condensation by-products in wet peroxide oxidation processes in the absence of a catalyst but in presence of oxygen to the treatment of phenol. The authors proposed different equations to fit the experimental data. The models of pseudo-first-order, Langmuir-Hinshelwood-Hougen-Watson (LHHW), and autocatalytic rate were tested. However, the first two models did not consider the presence of an induction period in the concentration profiles of the three variables (phenol, H_2O_2, and TOC). On the other hand, the autocatalytic model provides a good fit because it takes into account the activity promoted by the condensation by-products formed during the reaction.

Najjar et al. [79] performed oxidation by ozonation and H_2O_2/UV processes to treat paracetamol in a concentration of 100 $mg \cdot L^{-1}$. The second-order rate constant for the reaction of PCM with ozone was determined at pH 7.2 ($k_{O3/PRM}$ = 2.57 10^{-6} $L \cdot mmol^{-1} \cdot s^{-1}$). Hydroquinone and two other ozonation transformation products were identified by LC/UV, LC/MS, and MS/MS analyses

Hassani et al. [19] reported the synthesis of monodisperse cobalt ferrite NPs via assisted high-temperature thermal decomposition method and their assembly on reduced graphene oxide (rGO) to produce $CoFe_2O_4$-rGO nanocomposites, which displayed heterogeneous sono-Fenton-like processes for the removal of organic dyes from aqueous solution under ultrasonic irradiation. The maximum removal was 90.5% at pH 3 using 80 $mg \cdot L^{-1}$ of catalyst, 3 mM of H_2O_2, and 10 $mg \cdot L^{-1}$ of AO7 dye under a 350 W ultrasonic power in 120 min of reaction time. Experimental results revealed that the kinetics of the removal process could be described using a Langmuir-Hinshelwool (L-H) kinetic model.

4.3.2 Total Organic Carbon abatement rate

After completing a review of different methods to describe TOC kinetics [13,54,80–82], a model was proposed considering the total TOC as the sum of the different compounds produced during CWPO, as defined in Eq. 21.

$$TOC = TOC_A + TOC_B + TOC_C \quad (21)$$

where TOC_A corresponds to the initial pollutant (paracetamol), TOC_B corresponds to the oxidized intermediates resulting from the initial pollutant, which are still oxidized to refractory compounds represented by TOC_C. Specifically, TOC_C represents those compounds that do not oxidize and remain in the reaction medium. A reaction pathway was then proposed as given in Eq. 22.

$$\begin{array}{ccccc} & & \xrightarrow{} CO_2 & & \xrightarrow{} CO_2 \\ TOC_A + H_2O_2 & \xrightarrow{k_1 \; k_2} & TOC_B + H_2O_2 & \xrightarrow{k_3 \; k_4} & TOC_C \end{array} \quad (22)$$

In the case of TOC_A, the kinetic equation obtained previously must be used. Hence, equations 23 to 26 represent the reaction pathway.

$$\frac{dC_{H_2O_2}}{dt} = - k_{H_2O_2} C_{H_2O_2}{}^2 \quad (23)$$

$$\frac{dC_{TOC,A}}{dt} = - k_1 C_{TOC,A} (C_0 - C_{TOC,A}) C_{H_2O_2} \quad (24)$$

$$\frac{dC_{TOC,B}}{dt} = k_2 C_{TOC,A} (C_0 - C_{TOC,A}) C_{H_2O_2} - k_3 C_{TOC,B} C_{H_2O_2} \quad (25)$$

$$\frac{dC_{TOC,C}}{dt} = k_4 C_{TOC,B} C_{H_2O_2} \quad (26)$$

To solve this model, the initial limit of integration was considered at $t = 0$, $TOC_{A,0} = TOC_0$, $TOC_A = TOC_{PCM}$, $TOC_{B,0} = 0$ and $TOC_{C,0} = 0$. All calculations were performed using the python software. The kinetics constants k_{H2O2}, k_1, and C_0 have been previously determined. To perform the TOC kinetics model, the values of the constants used are obtained in the model N°8.

Figure 23 shows the experimental and fitted data recorded by the proposed method. The calculated determination factor R^2 was 0.98 and the SSE equals 0.18.

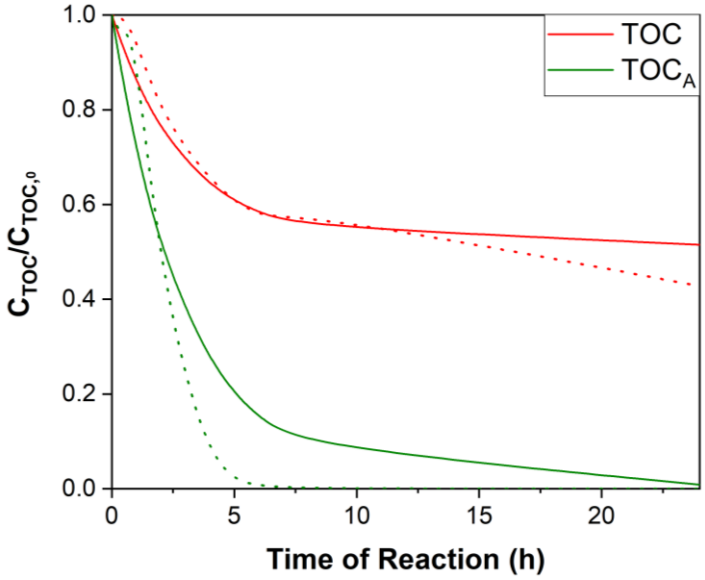

Figure 23. Experimental (dot lines) and predicted (lines) concentrations of TOC

As expected, the TOC_A referred to paracetamol is just a part of the total TOC. The calculated constants obtained are represented in Table 5.

Table 5. Values calculated for the proposed model.

Parameters	Values
k_2	3.51 10^{-3} $L^2 \cdot (mmol^2)^{-1} \cdot min^{-1}$
k_3	8.71 10^{-7} $L \cdot mmol^{-1} \cdot min^{-1}$
k_4	1.26 10^{-6} $L \cdot mmol^{-1} \cdot min^{-1}$

There are many approaches in how to describe a TOC kinetic model as those cited in the following. However, to the best of our knowledge, there are no other works that describe the kinetic model of concentration profiles of the TOC in the treatment of paracetamol by CWPO.

Audino et al. [86] conducted a study on photo-induced oxidation for the treatment of 0.26 $mmol \cdot L^{-1}$ of paracetamol in a deionized water matrix, during a reaction span of 200 min. The authors fit the TOC concentration profile in a semi-empirical model. The semi-empirical model refers to a model that represents a balanced approach between detailed first-principles modeling and pure empirical modeling. The calculated constant k was 0.03 min^{-1} and the mineralization value was 77%.

Diaz de Tuesta et. al. [81] developed a kinetic model with a commercial carbon black as a catalyst to describe the rate of H_2O_2 consumption and the targeted pollutant phenol degradation. The authors also took into account the total TOC as the sum of the different compounds produced during CWPO. Direct mineralization of phenol and the important selectivity of aromatic intermediates for mineralization have been reported instead of conversion into carboxylic acids as typically considered in wet oxidation studies of phenol.

Sun et al. [87] developed a generalized kinetic model for Electro-assisted catalytic wet air oxidation (ECWAO) for the treatment of triclosan (TCS) in wastewater. A general kinetic model, based on the depletion of TOC as a lumped parameter, is developed to adequately describe the k_{TOC} as a function of operating parameters. Under the optimal conditions, TCS was mineralized with efficiencies of 92 ± 1.5%.

Chapter 5: Conclusions and Future Research

5 Conclusions and Future Research

5.1 Conclusions

Based on the premise of optimizing yolk-shell magnetic nanoparticles for application as catalysts in catalytic wet peroxide oxidation, this thesis considered the synthesis of $CoFe_2O_4$@void@C materials. XRD, TEM, and FTIR analysis revealed that the core is composed by a $CoFe_2O_4$ cubic spinel structure with space group Fd-3m, with a crystallite size of 53 nm, calculated using the W-H method which is in agreement with the average size observed by TEM (53.51 ± 4.2 nm). The average size of the hybrid coated ferrite nanoparticles increases to 58.7 ± 8.1 nm due to the coating introduced.

The treatment of waters containing paracetamol is promising when considering the CWPO process with $CoFe_2O_4$@void@C as a catalyst. The CWPO runs conducted revealed that over half of the paracetamol is converted in less than two hours of reaction at the operating conditions of 80 °C, C_{cat} = 2.5 g·L^{-1} and $C_{paracetamol}$ = 100 mg·L^{-1}. During the oxidation reactions, it was possible to provide an excellent recovery of the catalyst. For the 0.25 g of catalyst applied in each run, it was possible to recover approximately 0.246 g using a magnetic field. The CWPO of paracetamol with $CoFe_2O_4$@void@C lead to a mineralization value of 58%. The hybrid material succeeds in avoid iron leaching and proved to be a stable catalyst, the amount of iron at the end of the reaction being equal to 1.59 mg·L^{-1}, which is within the limit concentration of 2 mg·L^{-1} of iron in water, established by the European Union laws.

The CWPO of PCM with the $CoFe_2O_4$@void@C catalyst can be well-described by an empirical kinetic model composed of a second-order and an autocatalytic expression to describe the decomposition of H_2O_2 and PCM, respectively. In this sense, it is possible to predict the induction period, which takes place in the process. The kinetic model of TOC can be well-described as the sum of the initial pollutant plus the oxidation intermediates from the PCM and the organic components that are refractory to the process.

5.2 Future Research

A complementary work that could be done with the $CoFe_2O_4$@void@C catalyst is its application as a catalyst in the CWPO of other contaminants of emerging concern, such as ibuprofen, nitrophenol, and chlorophenol, among others. It is also important to test other samples of the hybrid coated ferrite with the same procedure, but with a lower time of calcination, to test whether or not the material maintains the same magnetic behavior.

References

REFERENCES

1. Ribeiro, R. S. *et al.* Hybrid magnetic graphitic nanocomposites towards catalytic wet peroxide oxidation of the liquid effluent from a mechanical biological treatment plant for municipal solid waste. *Appl. Catal. B Environ.* **219**, 645–657 (2017).
2. Ribeiro, R. S. *et al.* Enhanced performance of cobalt ferrite encapsulated in graphitic shell by means of AC magnetically activated catalytic wet peroxide oxidation of 4-nitrophenol. *Chem. Eng. J.* **376**, 120012 (2018).
3. Giannakopoulou, T., Kompotiatis, L., Kontogeorgakos, A. & Kordas, G. Microwave behavior of ferrites prepared via sol-gel method. *J. Magn. Magn. Mater.* **246**, 360–365 (2002).
4. Pullar, R. C. Hexagonal ferrites: A review of the synthesis, properties and applications of hexaferrite ceramics. *Prog. Mater. Sci.* **57**, 1191–1334 (2012).
5. Kim, K. N., Jung, H. R. & Lee, W. J. Hollow cobalt ferrite-polyaniline nanofibers as magnetically separable visible-light photocatalyst for photodegradation of methyl orange. *J. Photochem. Photobiol. A Chem.* **321**, 257–265 (2016).
6. Senapati, K. K., Borgohain, C. & Phukan, P. $CoFe_2O_4$-ZnS nanocomposite: A magnetically recyclable photocatalyst. *Catal. Sci. Technol.* **2**, 2361–2366 (2012).
7. Heidari, M. R. *et al.* Photo-Fenton like catalyst system: Activated Carbon/$CoFe_2O_4$ nanocomposite for reactive dye removal from textile wastewater. *Appl. Sci.* **9**(5), 963 (2019).
8. Rodrigues, O. R. *et al.* A Tailor-made protocol to synthesize yolk-shell graphene-based magnetic nanoparticles for nanomedicine. *Journal of Carbon Research C.* **4,** 55, 4040055 (2018).
9. Rodrigues, R. O. *et al.* Multifunctional graphene-based magnetic nanocarriers for combined hyperthermia and dual stimuli-responsive drug delivery. *Mater. Sci. Eng. C.* **93**, 206–217 (2018).
10. Schultz-Sikma, E. A. *et al.* Probing the chemical stability of mixed ferrites: Implications for magnetic resonance contrast agent design. *Chem. Mater.* **23**, 2657–2664 (2011).
11. Pottker, W. E. *et al.* Influence of order-disorder effects on the magnetic and optical properties of $NiFe_2O_4$ nanoparticles. *Ceram. Int.* **44**, 17290–17297 (2018).
12. La Porta, F. A. *et al.* Correlation between structural and electronic order-disorder

effects and optical properties in ZnO nanocrystals. *J. Mater. Chem. C.* **2**, 10164–10174 (2014).

13. Ianoş, R. *et al.* Combustion synthesis of iron oxide/carbon nanocomposites, efficient adsorbents for anionic and cationic dyes removal from wastewaters. *J. Alloys Compd.* **741**, 1235–1246 (2018).
14. Thoda, O., Xanthopoulou, G., Vekinis, G. & Chroneos, A. The effect of the precursor solution's pretreatment on the properties and microstructure of the SCS final nanomaterials. *Appl. Sci.* **9**, 1200 (2019).
15. Kakihana, M. 'Sol-Gel' preparation of high temperature superconducting oxides. *J. Sol-Gel Sci. Technol.* **6**, 7–55 (1996).
16. Cividanes, L. S., Campos, T. M. B., Rodrigues, L. A., Brunelli, D. D. & Thim, G. P. Review of mullite synthesis routes by sol-gel method. *J. Sol-Gel Sci. Technol.* **55**, 111–125 (2010).
17. Ribeiro, R. S., Silva, A. M. T., Figueiredo, J. L., Faria, J. L. & Gomes, H. T. Catalytic wet peroxide oxidation: A route towards the application of hybrid magnetic carbon nanocomposites for the degradation of organic pollutants. A review. *Appl. Catal. B Environ.* **187**, 428–460 (2016).
18. Oliveira, J. *et al.* Carbon-based magnetic nanocarrier for controlled drug release: A green synthesis approach. *Journal of Carbon Research C.* **5**, 5010001 (2018).
19. Hassani, A. *et al.* Heterogeneous sono-Fenton-like process using magnetic cobalt ferrite-reduced graphene oxide ($CoFe_2O_4$-rGO) nanocomposite for the removal of organic dyes from aqueous solution. *Ultrason. Sonochem.* **40**, 841–852 (2018).
20. Ribeiro, A. R., Nunes, O. C., Pereira, M. F. R. & Silva, A. M. T. An overview on the advanced oxidation processes applied for the treatment of water pollutants defined in the recently launched Directive 2013/39/EU. *Environ. Int.* **75**, 33–51 (2015).
21. Munoz, M., de Pedro, Z. M., Casas, J. A. & Rodriguez, J. J. Preparation of magnetite-based catalysts and their application in heterogeneous Fenton oxidation - A review. *Appl. Catal. B Environ.* **176**–**177**, 249–265 (2015).
22. Olsson, R. T. *et al.* Controlled synthesis of near-stoichiometric cobalt ferrite nanoparticles. *Chem. Mater.* **17**, 5109–5118 (2005).
23. Braun, T., Schubert, A. & Zsindely, S. Nanoscience and nanotechnology on the balance. *Scientometrics.* **38**, 321–325 (1997).

24. Behrens, S. & Appel, I. Magnetic nanocomposites. *Curr. Opin. Biotechnol.* **39**, 89–96 (2016).
25. Sanvicens, N. & Marco, M. P. Multifunctional nanoparticles - properties and prospects for their use in human medicine. *Trends Biotechnol.* **26**, 425–433 (2008).
26. Baldissera, M. R. *et al.* Síntese e caracterização de ferritas de Zn e Mn provenientes de pilhas inutilizadas. *Ceramica* **60**, 52–56 (2014).
27. Zhang, Y. *et al.* The temperature dependence of magnetic properties for cobalt ferrite nanoparticles by the hydrothermal method. *J. Appl. Phys.* **108**, 084312 (2010)
28. Maaz, K., Mumtaz, A., Hasanain, S. K. & Ceylan, A. Synthesis and magnetic properties of cobalt ferrite ($CoFe_2O_4$) nanoparticles prepared by wet chemical route. *J. Magn. Magn. Mater.* **308**, 289–295 (2007).
29. Zhao, D., Wu, X., Guan, H. & Han, E. Study on supercritical hydrothermal synthesis of $CoFe_2O_4$ nanoparticles. *J. Supercrit. Fluids* **42**, 226–233 (2007).
30. Hajalilou, A. & Mazlan, S. A. A review on preparation techniques for synthesis of nanocrystalline soft magnetic ferrites and investigation on the effects of microstructure features on magnetic properties. *Appl. Phys. A Mater. Sci. Process.* **122**, (2016).
31. Silva, F. C. Síntese, caracterização e estudo de propriedades magnéticas de ferritas mistas $Co_{1-x}Mg_xFe_2O_4$ ($0 \leq x \leq 0,6$). **4**, 94 (2011).
32. Valant, M., Axelsson, A. K., Aguesse, F. & Alford, N. M. Molecular auxetic behavior of epitaxial co-ferrite spinel thin film. *Adv. Funct. Mater.* **20**, 644–647 (2010).
33. Hashemi, S. M., Hasani, S., Jahanbani Ardakani, K. & Davar, F. The effect of simultaneous addition of ethylene glycol and agarose on the structural and magnetic properties of $CoFe_2O_4$ nanoparticles prepared by the sol-gel auto-combustion method. *J. Magn. Magn. Mater.* **492**, 165714 (2019).
34. Gan, L., Shang, S., Yuen, C. W. M., Jiang, S. X. & Hu, E. Hydrothermal synthesis of magnetic $CoFe_2O_4$/graphene nanocomposites with improved photocatalytic activity. *Appl. Surf. Sci.* **351**, 140–147 (2015).
35. García-Cerda, L. A., Torres-García, V. A., Matutes-Aquino, J. A. & Ayala-Valenzuela, O. E. Magnetic nanocomposites: Preparation and characterization of Co-ferrite nanoparticles in a silica matrix. *J. Alloys Compd.* **369**, 148–151 (2004).

36. Wang, X., Zhuang, J., Peng, Q. & Li, Y. A general strategy for nanocrystal synthesis. *Nature.* **437**, 121–124 (2005).
37. Suresh, S. *et al.* Evaluation of corrosion resistance of nano nickel ferrite and magnetite double layer coatings on carbon steel. *Thin Solid Films.* **645**, 77–86 (2018).
38. Hao, Z., Liu, Q. F. & Wang, J. B. Coating carbon nanotubes with ferrites using an improved co-precipitation method. *J. Compos. Mater.* **44**, 389–395 (2010).
39. Smuleac, V., Varma, R., Sikdar, S. & Bhattacharyya, D. Green synthesis of Fe and Fe/Pd bimetallic nanoparticles in membranes for reductive degradation of chlorinated organics. *J. Memb. Sci.* **379**, 131–137 (2011).
40. Rahman, I. A. & Padavettan, V. Synthesis of Silica nanoparticles by sol-gel: Size-dependent properties, surface modification, and applications in silica-polymer nanocompositesa review. *J. Nanomater.* **2012**, 132424 (2012).
41. Sinkó, K., Mezei, R. & Zrínyi, M. Gelation of aluminosilicate systems under different chemical conditions 18. *J. Sol-Gel Sci. Technol.* **21**, 147–156 (2001).
42. Lu, A. H., Salabas, E. L. & Schüth, F. Magnetic nanoparticles: Synthesis, protection, functionalization, and application. *Angew. Chemie - Int. Ed.* **46**, 1222–1244 (2007).
43. Purbia, R. & Paria, S. Yolk/shell nanoparticles: Classifications, synthesis, properties, and applications. *Nanoscale.* **7**, 19789–19873 (2015).
44. Liu, L. *et al.* Self-assembled hierarchical yolk-shell structured NiO@C from metal-organic frameworks with outstanding performance for lithium storage. *Chem. Commun.* **50**, 9485–9488 (2014).
45. Liu, L. *et al.* Self-assembled hierarchical yolk-shell structured NiO@C from metal-organic frameworks with outstanding performance for lithium storage. *Chem. Commun.* **50**, 9485–9488 (2014).
46. Fuertes, A. B., Valle-Vigón, P. & Sevilla, M. One-step synthesis of silica@resorcinol-formaldehyde spheres and their application for the fabrication of polymer and carbon capsules. *Chem. Commun.* **48**, 6124–6126 (2012).
47. Liu, J. *et al.* Extension of the Stöber method to the preparation of monodisperse resorcinol-formaldehyde resin polymer and carbon spheres. *Angew. Chemie - Int. Ed.* **50**, 5947–5951 (2011).
48. Zhu, Y. *et al.* Strategies for enhancing the heterogeneous fenton catalytic

reactivity: A review. *Appl. Catal. B Environ.* **255**, 117739 (2019).

49. Tabrizi, G. B. & Mehrvar, M. Integration of advanced oxidation technologies and biological processes: Recent developments, trends, and advances. *J. Environ. Sci. Heal. - Part A Toxic/Hazardous Subst. Environ. Eng.* **39**, 3029–3081 (2004).
50. Liotta, L. F., Gruttadauria, M., Di Carlo, G., Perrini, G. & Librando, V. Heterogeneous catalytic degradation of phenolic substrates: Catalysts activity. *J. Hazard. Mater.* **162**, 588–606 (2009).
51. Bethi, B., Sonawane, S. H., Bhanvase, B. A. & Gumfekar, S. P. Nanomaterials-based advanced oxidation processes for wastewater treatment: A review. *Process Intensif.* **109**, 178–189 (2016).
52. Rueda-Márquez, J. J., Sillanpää, M., Pocostales, P., Acevedo, A. & Manzano, M. A. Post-treatment of biologically treated wastewater containing organic contaminants using a sequence of H_2O_2 based advanced oxidation processes: Photolysis and catalytic wet oxidation. *Water Res.* **71**, 85–96 (2015).
53. Gogate, P. R. & Pandit, A. B. A review of imperative technologies for wastewater treatment II: Hybrid methods. *Adv. Environ. Res.* **8**, 553–597 (2004).
54. De Morais, J. L. & Zamora, P. P. Use of advanced oxidation processes to improve the biodegradability of mature landfill leachates. *J. Hazard. Mater.* **123**, 181–186 (2005).
55. Fioreze, M., Santos, E. P. dos & Schmachtenberg, N. Processos oxidativos avançados: Fundamentos e aplicação ambiental. *Rev. Eletrônica em Gestão, Educ. e Tecnol. Ambient.* **18**, 79–91 (2014).
56. Sun, S. P., Zeng, X. & Lemley, A. T. Nano-magnetite catalyzed heterogeneous Fenton-like degradation of emerging contaminants carbamazepine and ibuprofen in aqueous suspensions and montmorillonite clay slurries at neutral pH. *J. Mol. Catal. A Chem.* **371**, 94–103 (2013).
57. Wang, H. *et al.* Fe_3O_4-MWCNT magnetic nanocomposites as efficient peroxidase mimic catalysts in a Fenton-like reaction for water purification without pH limitation. *RSC Adv.* **4**, 45809–45815 (2014).
58. Diaz de Tuesta, J. L. *et al.* Janus amphiphilic carbon nanotubes as Pickering interfacial catalysts for the treatment of oily wastewater by selective oxidation with hydrogen peroxide. *Catal. Today.* **356**, 205-215 (2019).
59. Silva, A. S., Kalmakhanova, M. S., Massalimova, B. K., de Tuesta, J. L. D. &

Gomes, H. T. Wet peroxide oxidation of paracetamol using acid activated and Fe/Co-pillared clay catalysts prepared from natural clays. *Catalysts.* **9**, 705 (2019).

60. Velichkova, F., Julcour-Lebigue, C., Koumanova, B. & Delmas, H. Heterogeneous Fenton oxidation of paracetamol using iron oxide nanoparticles. *J. Environ. Chem. Eng.* **1**, 1214–1222 (2013).
61. Al-kaf, A., Naji, K. M., Abdullah, Q. Y. M. & Edrees, W. Occurrence of paracetamol in aquatic environments and transformation by microorganisms : A Review. *Chronicles of pharmaceutical science.* **1.6**, 341-355 (2017).
62. Alalm, M. G., Tawfik, A. & Ookawara, S. Degradation of four pharmaceuticals by solar photo-Fenton process: Kinetics and costs estimation. *J. Environ. Chem. Eng.* **3**, 46–51 (2015).
63. Carrasco-Díaz, M. R., Castillejos-López, E., Cerpa-Naranjo, A. & Rojas-Cervantes, M. L. Efficient removal of paracetamol using $LaCu_{1-x}M_xO_3$ (M = Mn, Ti) perovskites as heterogeneous Fenton-like catalysts. *Chem. Eng. J.* **304**, 408–418 (2016).
64. Masso, C. M. Valorization of compost in the production of carbon-based materials for the treatment of contaminated wastewater. (Instituto Politécnico de Bragança, Bragança, 2018)
65. Hall, W. H. X-ray line broadening in metals. *Proc. Phys. Soc. A*. **62**, 741–743 (1949).
66. Nath, D., Singh, F. & Das, R. X-ray diffraction analysis by Williamson-Hall, Halder-Wagner and size-strain plot methods of CdSe nanoparticles- a comparative study. *Mater. Chem. Phys.* **239**, 122021 (2020).
67. Warren, B. E. & Averbach, B. L. The separation of cold-work distortion and particle size broadening in x-ray patterns. *J. Appl. Phys.* **23**, 497 (1952).
68. Balzar, D. & Ledbetter, H. Voigt-function modeling in Fourier analysis of size- and strain-broadened X-ray diffraction peaks. *J. Appl. Crystallogr.* **26**, 97–103 (1993).
69. Neumann, B. *et al.* Sol-gel preparation of alumina stabilized rare earth areo- and xerogels and their use as oxidation catalysts. *J. Colloid Interface Sci.* **422**, 71–78 (2014).
70. Bertoncini, M., Coelho, L. A. F., Maciel, I. O. & Pezzin, S. H. Purification of single-wall carbon nanotubes by heat treatment and supercritical extraction. *Mater.*

Res. **14**, 380–383 (2011).

71. Fernández, A., Peretyagin, P., Solís, W., Torrecillas, R. & Borrell, A. Functionalization of carbon nanofibres obtained by floating catalyst method. *J. Nanomater.* **2015**, 395014 (2015).
72. Hussain, A., Abbas, T. & Niazi, S. B. Preparation of $Ni_{1-x}Mn_xFe_2O_4$ ferrites by sol-gel method and study of their cation distribution. *Ceram. Int.* **39**, 1221–1225 (2013).
73. Ribeiro, R. S. *et al.* Screening of heterogeneous catalysts for the activated persulfate oxidation of sulfamethoxazole in aqueous matrices. Does the matrix affect the selection of catalyst?. *J. Chem. Technol. Biotechnol.* **94**, 2425–2432 (2019).
74. Desai, S. S. *et al.* Influence of Zn-Zr substitution on the crystal chemistry and magnetic properties of $CoFe_2O_4$ nanoparticles synthesized by sol-gel method. *Phys. B Condens. Matter* **596**, 412400 (2020).
75. Ai, L. & Jiang, J. Influence of annealing temperature on the formation, microstructure and magnetic properties of spinel nanocrystalline cobalt ferrites. *Curr. Appl. Phys.* **10**, 284–288 (2010).
76. Bagade, A. A. *et al.* Assessment of structural, morphological, magnetic and gas sensing properties of $CoFe_2O_4$ thin films. *Journal of Colloid and Interface Science.* **497** 181-192 (2017).
77. Habibi, M. H. & Parhizkar, H. J. FTIR and UV-vis diffuse reflectance spectroscopy studies of the wet chemical (WC) route synthesized nano-structure $CoFe_2O_4$ from $CoCl_2$ and $FeCl_3$. *Spectrochim. Acta - Part A Mol. Biomol. Spectrosc.* **127**, 102–106 (2014).
78. Wang, B., Gao, C., Wang, W., Kong, F. & Zheng, C. TGA-FTIR investigation of chemical looping combustion by coal with $CoFe_2O_4$ combined oxygen carrier. *J. Anal. Appl. Pyrolysis.* **105**, 369–378 (2014).
79. Hamdi El Najjar, N., Touffet, A., Deborde, M., Journel, R. & Karpel Vel Leitner, N. Kinetics of paracetamol oxidation by ozone and hydroxyl radicals, formation of transformation products and toxicity. *Sep. Purif. Technol.* **136**, 137–143 (2014).
80. Diaz de Tuesta, J. L. *et al.* The pH effect on the kinetics of 4-nitrophenol removal by CWPO with doped carbon black catalysts. *Catal. Today.* **356,** 216-225 (2020).
81. Diaz de Tuesta, J. L., Quintanilla, A., Casas, J. A. & Rodriguez, J. J. Kinetic

modeling of wet peroxide oxidation with a carbon black catalyst. *Appl. Catal. B Environ.* **209**, 701–710 (2017).

82. Diaz de Tuesta, J. L.Figueruelo, C. & Munoz, M. Condensation by-products in wet peroxide oxidation: Fouling or catalytic promotion? Part I: Evidences of an autocatalytic process. *Catalysts.* **9**, 516 (2019)
83. Process, A., Diaz de Tuesta, J. L., Figueruelo, C. & Munoz, M. Condensation by-products in wet peroxide oxidation: Fouling or catalytic promotion? Part II: Activity, nature and stability. *Catalysts.* **9**, 518 (2019).
84. Enterría, M. & Figueiredo, J. L. Nanostructured mesoporous carbons: Tuning texture and surface chemistry. *Carbon N. Y.* **108**, 79–102 (2016).
85. Van, H. T. *et al.* Heterogeneous Fenton oxidation of paracetamol in aqueous solution using iron slag as a catalyst: Degradation mechanisms and kinetics. *Environ. Technol. Innov.* **18**, 100670 (2020).
86. Audino, F., Santamaria, J. M. T., Del Valle Mendoza, L. J., Graells, M. & Pérez-Moya, M. Removal of paracetamol using effective advanced oxidation processes. *Int. J. Environ. Res. Public Health.* **16**, 505 (2019).
87. Sun, M., Hong, X. H., Tao, X. F., Zhai, L. F. & Wang, S. A generalized kinetic model for electro-assisted catalytic wet air oxidation of triclosan on Ni@NiO/graphite electrode. *Chem. Eng. Sci.* **222**, 115696 (2020).

ANNEX A

Figure I – Magnetic stirring plate IKA® C-MAG HS 7 with temperature control IKA® ETS-D5

Figure II – Electric muffle furnaces, N-8 L

Figure III – Ultrasounds – H, P-Selecta

Figure IV – Vertical tubular furnace ROS 50/250/12, Thermoconcept

Figure V – T70 UV-Vis spectrophotometer, PG Instruments Ltd

Figure VI – HPLC High performance liquid chromatography

Figure VII - Total Organic Carbon - SHIMADZU TOC

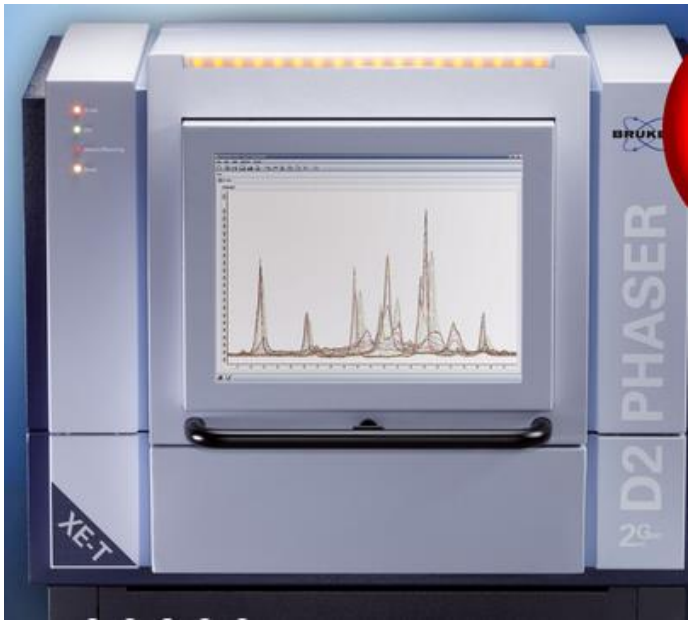

Figure VIII - XRD / Bruker D8 Discover diffractometer